

# Influence of Physical Factors on Restratification of the Upper Water Column in Antarctic Coastal Polynyas

Yilang Xu<sup>1,2,\*</sup>, Weifeng (Gordon) Zhang<sup>1</sup>, Ted Maksym<sup>1</sup>, Rubao Ji<sup>3</sup>, Yun Li<sup>4</sup>, Catherine Walker<sup>1</sup>

<sup>1</sup> *Applied Ocean Physics and Engineering Department, Woods Hole Oceanographic Institution, Woods Hole, Massachusetts, United States*

<sup>2</sup> *MIT-WHOI Joint Program in Oceanography/Applied Ocean Science and Engineering, Cambridge, Massachusetts, United States*

<sup>3</sup> *Biology Department, Woods Hole Oceanographic Institution, Woods Hole, Massachusetts, United States*

<sup>4</sup> *School of Marine Science and Policy, University of Delaware, Lewes, Delaware, United States*

\* Corresponding author: Yilang Xu ([yilangxu@mit.edu](mailto:yilangxu@mit.edu))

Manuscript accepted in *Journal of Geophysical Research: Oceans* (February 2024)

Preprint available at <https://doi.org/10.22541/au.170179733.36188381/v1>

## Key Points:

- Biologically-important springtime near-surface restratification in Antarctic coastal polynyas varies spatially within a polynya.
- Sea ice meltwater from regions offshore of the polynya is the primary buoyancy source of polynya near-surface restratification.
- Ice shelf basal meltwater mixes over the water column during its ascent and contributes little to polynya near-surface restratification.

## Abstract

Antarctic coastal polynyas are hotspots of biological production with intensive springtime phytoplankton blooms that strongly depend on meltwater-induced restratification in the upper part of the water column. However, the fundamental physics that determine spatial inhomogeneity of the spring restratification remain unclear. Here, we investigate how different meltwaters affect springtime restratification and thus phytoplankton bloom in Antarctic coastal polynyas. A high-resolution coupled ice-shelf/sea-ice/ocean model is used to simulate an idealized coastal polynya similar to the Terra Nova Bay Polynya, Ross Sea, Antarctica. To evaluate the contribution of various meltwater sources, we conduct sensitivity simulations altering physical factors such as alongshore winds, ice shelf basal melt, and surface freshwater runoff. Our findings indicate that sea ice meltwater from offshore is the primary buoyancy source of polynya near-surface restratification, particularly in the outer-polynya region where chlorophyll concentration tends to be high. Downwelling-favorable alongshore winds can direct offshore sea ice away and prevent sea ice meltwater from entering the polynya region. Although the ice shelf basal meltwater can ascend to the polynya surface, much of it is mixed vertically over the water column and confined horizontally to a narrow coastal region, and thus does not contribute significantly to the polynya near-surface restratification. Surface runoff from ice shelf surface melt could contribute greatly to the polynya near-surface restratification. Nearby ice tongues and headlands strongly influence the restratification through modifying polynya circulation and meltwater transport pathways. Results of this study can help explain observed spatiotemporal variability in restratification and associated biological productivity in Antarctic coastal polynyas.

## **Plain Language Summary**

Antarctic coastal polynyas are key habitats of regional marine ecosystems. During spring, the upper part of the polynya water column restratifies and forms a near-surface layer of low-salinity water. This process is important for springtime phytoplankton blooms, as the stable surface layer keeps phytoplankton in the well-lit region and enhances phytoplankton growth. Employing high-resolution models of idealized coastal polynyas, this work unravels the spatial variation of restratification processes in a polynya and investigates the physical factors that affect them. It shows that sea ice meltwater from offshore regions is the foremost contributor to the near-surface restratification in a polynya. Meanwhile, low-salinity water from basal melt of a neighboring floating ice shelf contributes little to the near-surface restratification in a polynya because much of the meltwater mixes vertically with ambient waters as it rises. This is in contrast to the sea ice meltwater being directly injected into the ocean surface. Freshwater runoff from the surface melt of an ice shelf is also directly injected into the polynya surface. However, due to earth rotation, it is often confined in a narrow coastal region next to the ice shelf and thus does not contribute to restratification in most of the polynya area.

## 1. Introduction

Antarctic coastal polynyas are key habitats of Antarctic ecosystems and a major source of the Antarctic Bottom Water (Morales Maqueda et al., 2004; Smith & Barber, 2007), which is the lowest branch of global overturning circulation and occupies the abyssal layer of the global ocean. They are often characterized by deep wintertime mixing due to dense water formation from sea ice production (Morales Maqueda et al., 2004) and elevated biological productivity associated with spring restratification (Arrigo & van Dijken, 2003; Arrigo et al., 2015). In winter, nutrient-rich subsurface waters are brought up to the surface layer by strong vertical mixing within the polynya water column (Vaillancourt et al., 2003). In contrast, during spring, rising air temperatures and surface heating induce sea ice retreat and stabilize the water column, enabling phytoplankton blooms through enhanced light availability (Arrigo, 2007; Li et al., 2016). However, the timing and magnitude of these spring blooms exhibit considerable variability across different coastal polynyas (Arrigo & van Dijken, 2003; Li et al., 2016; Moreau et al., 2019). The onset of these spring blooms within polynyas is often associated with shoaling of the mixed layer, a process affected by input of relatively fresh water from sea ice melt (Arrigo & van Dijken, 2003; Moreau et al., 2019), coastal surface runoff (Bell et al., 2017; Bell et al., 2018), and glacial ice shelf basal melt influenced by Circumpolar Deep Water (CDW) intrusion into the ice shelf cavity (Silvano et al., 2018). It has been suggested that the low-density meltwaters from sea ice and glaciers can accumulate in the surface layer and establish stratification in the upper part of the polynya water column (Randall-Goodwin et al., 2015; Schofield et al., 2018; Silvano et al., 2018). The variance in these physical factors can likely generate distinct patterns of restratification in Antarctic coastal polynyas and modify the timing and intensity of phytoplankton blooms. Interestingly, studies suggest that the upwelling flow of the ice shelf basal meltwater at the ice shelf front could also lead to water column mixing (Alderkamp et al., 2015), opposing the presumptive role of basal meltwater in supporting stratification. Subsurface glacial meltwater can also be mechanically mixed into the upper layer of the ocean by wind activity or ice drift (Randall-Goodwin et al., 2015). Meanwhile, strong variability exists in the rates of glacial melt across Antarctica (Arrigo et al., 2015), making it challenging to systematically quantify the contribution of glacial melt to the springtime restratification in coastal polynyas. Nonetheless, the precise influence of the freshwater sources on the timing and magnitude of spring restratification in polynyas are not yet fully

understood. A thorough examination of the small-scale process of polynya springtime restratification is necessary.

In this study, we use the Terra Nova Bay Polynya (TNBP) as an example to qualitatively illustrate the inhomogeneous distribution of the meltwaters and their connection to the springtime restratification. Observations are used to depict the typical evolution of water column restratification in the TNBP, which is situated at the southwest corner of the Ross Sea and confined between a headland named Cape Washington to the north and Drygalski Ice Tongue to the south (Fig. 1a). Studies have shown active sea ice formation, intense brine rejection, vigorous dense water formation, and deep vertical mixing in the TNBP in the winter months (April–October), induced by strong offshore katabatic winds (Ackley et al., 2020; Budillon and Spezie, 2000; Rusciano et al., 2013). Meanwhile, satellite images of the region around the TNBP show that sea ice retreat during the spring months (November–January) in response to increasing air temperature and diminishing wind speed (Fig. 2a) exhibits a pronounced south-north asymmetry across the Drygalski Ice Tongue (Fig. 1b-g). The sea ice retreat is much more pronounced in the polynya region to the north of the ice tongue, while the sea ice coverage to the south remains largely intact till January. Notably, the retreat of the sea ice coverage to the north of the ice tongue in spring primarily occurs in the northeastward direction (Fig. 1b-g), consistent with the prevailing wind direction, as measured at the Manuela Automatic Weather Station on the coast of the TNBP (Fig. 2d). In situ shipboard measurements during the *Polynyas, Ice Production, and seasonal Evolution in the Ross Sea* (PIPERS) project field campaign in winter 2017 (Ackley et al., 2020) show a largely homogenized water column resulting from the deep wintertime vertical mixing (Fig. 3). This homogenization of the water column presumably occurs in every winter. Meanwhile, measurements performed by instrumented elephant seals (Roquet et al., 2014; Roquet et al., 2021) in the TNBP in March 2010 (summer) show a highly stratified water column with pronounced salinity and density gradients in the top 300 m and the highest gradients in the top 50 m (Fig. 3). The surface salinity was about 1.5 psu lower than salinity of the deep water. Due to the lack of observation, it is unclear how and when exactly the stratification was established. But it is likely that the upper-layer stratification was developed in the spring with the injection of the sea ice and ice shelf meltwaters.

Springtime restratification in the Antarctic coastal polynyas often coincides with large phytoplankton blooms. To demonstrate their association in the TNBP, Fig. 4 shows co-evolution

of sea ice concentration calculated by the ARTIST Sea Ice (ASI) algorithm (Spreen et al., 2008) and chlorophyll-a concentration measured by the NOAA Suomi-NPP VIIRS satellite in spring 2019. In the early spring (Fig. 4a-f), the expansion of the TNBP towards the northeast (i.e., the northeastward retreat of the sea ice) corresponds with high chlorophyll concentrations near the northeast edge of the polynya, marked by the 10% sea ice concentration contour. This inhomogeneous distribution of the phytoplankton bloom in the TNBP suggests a potential correlation between the sea ice retreat and enhanced phytoplankton growth. Note that the cut off of chlorophyll-a concentration at the ice edge is likely a choice during the satellite data processing, and possible sub-ice phytoplankton blooms are not included in the data. Considering the distribution of chlorophyll-a in the open region of the TNBP, it is possible that the localized sea ice melt at the polynya edge results in a spatially variable stratification and then inhomogeneous phytoplankton growth. As the season proceeds and more sea ice melts, chlorophyll-a concentration becomes more homogenized in the polynya (Fig. 4g-i). It is likely that stratification of the polynya water column at that time also becomes more horizontally homogeneous due to redistribution of the meltwater induced by winds and ocean circulation. These observations underscore the need to investigate the processes affecting freshwater input and restratification for a better understanding the phytoplankton bloom dynamics in the polynyas.

This study examines the physical factors that affect the timing and extent of the springtime restratification in the upper water column of Antarctic coastal polynyas, emphasizing the influence of the meltwaters and their three-dimensional distribution. We hypothesize that the distribution of the meltwaters is subject to the influence of local ocean circulation, which, in turn, is impacted by factors such as winds and coastline geometry. In the subsequent sections, an idealized ice-shelf/sea-ice/ocean coupled numerical model is employed to qualitatively examine the first-order dynamics of the springtime restratification. While the TNBP is used as an example to guide the design of the model, the dynamical insights drawn from the modeling analysis can be applied to a broad spectrum of Antarctic coastal polynyas.

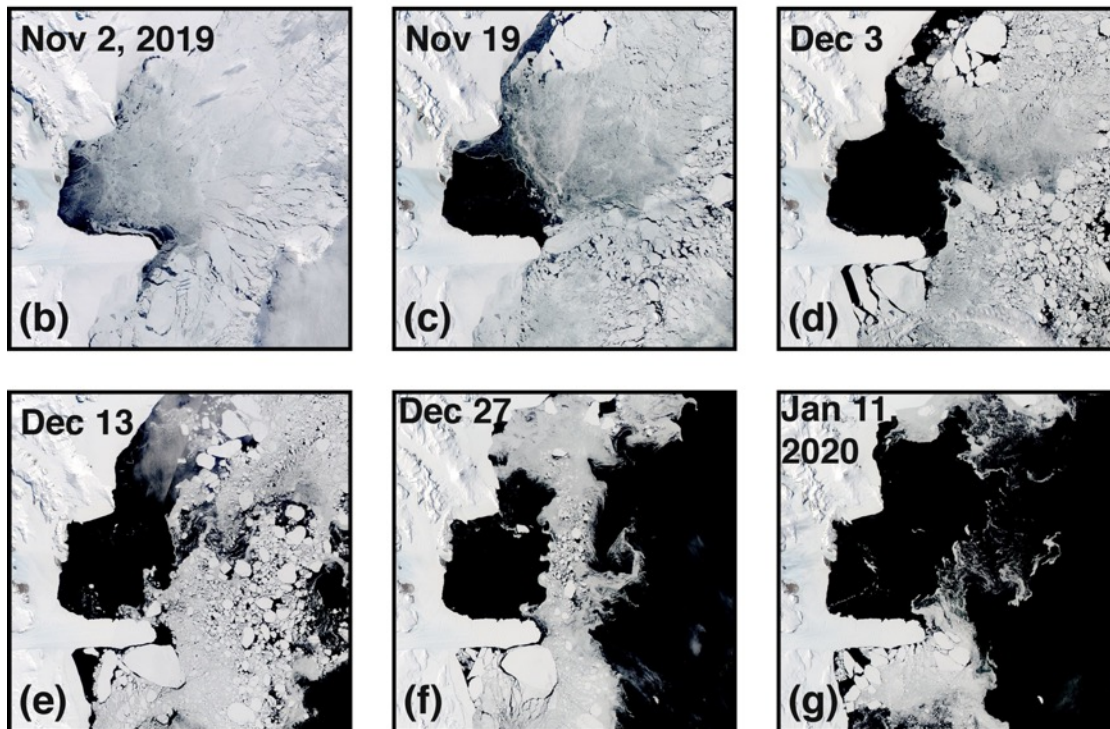
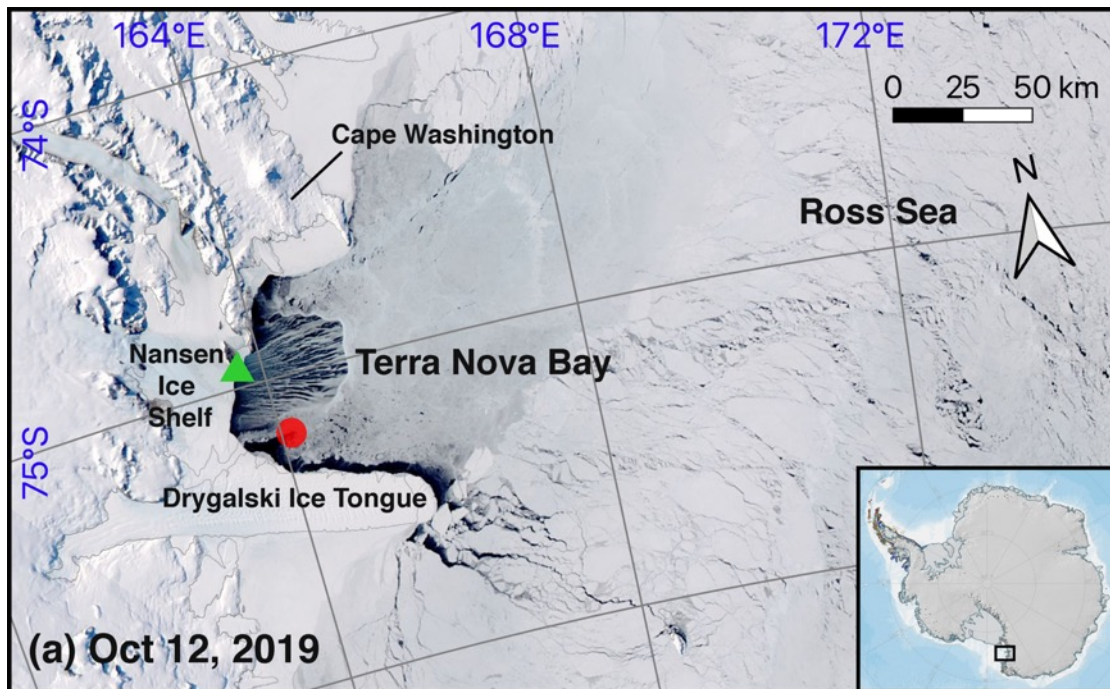


**Fig. 1.** Terra/Aqua MODIS satellite images of the Terra Nova Bay Polynya between October 2019 and January 2020. The green triangle denotes the location of the Manuela Automatic Weather Station. The red circle indicates the location of the PIPERS CTD cast on May 6, 2017.



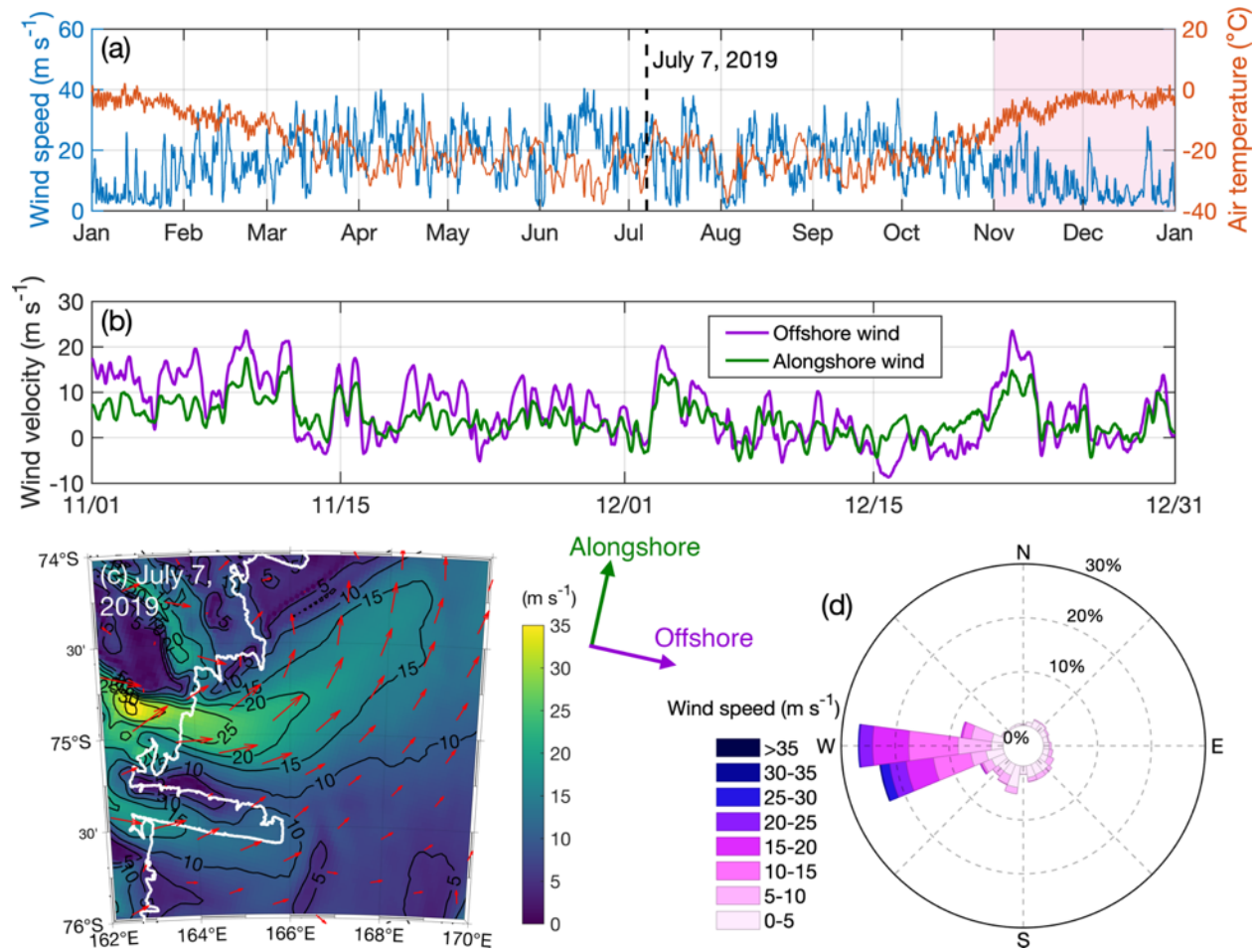


**Fig. 2.** Atmospheric conditions in the Terra Nova Bay Polynya: (a) wind speed and air temperature measured at the Manuela Automatic Weather Station in 2019; (b) time series of the decomposed offshore and alongshore winds in November and December of 2019; (c) a snapshot of the wind speed at 10-meters height on July 7, 2019 produced by the Antarctic Mesoscale Prediction System (Powers et al., 2012); (d) a wind rose plot of the wind speed and the direction it comes from in November and December of 2019. In (a), the dashed line denotes the date of the data shown in (c) and the pink shade highlights the early spring of 2019 (November and December). The coastline in (c) is obtained from the GSHHG data set (Wessel & Smith, 1996). The alongshore direction in (c) is defined as 24 degrees (clockwise) from the true north.



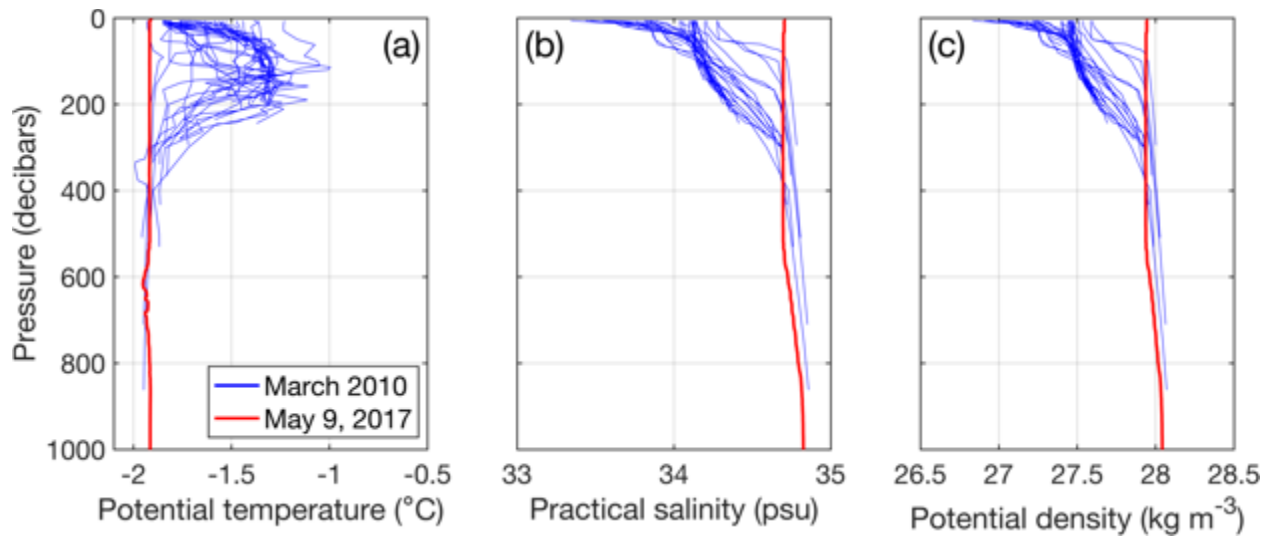


**Fig 3.** (a) Potential temperature, (b) practical salinity, and (c) potential density profiles recorded in the Terra Nova Bay Polynya. The blue lines are measured by instrumented elephant seals (Roquet et al., 2014; Roquet et al., 2021) between 163–165°E, 74.8–75.3°S during March 2010. The red lines are obtained from PIPERS CTD cast on May 9, 2017 (Ackley et al., 2020; see Fig. 1a for its location).

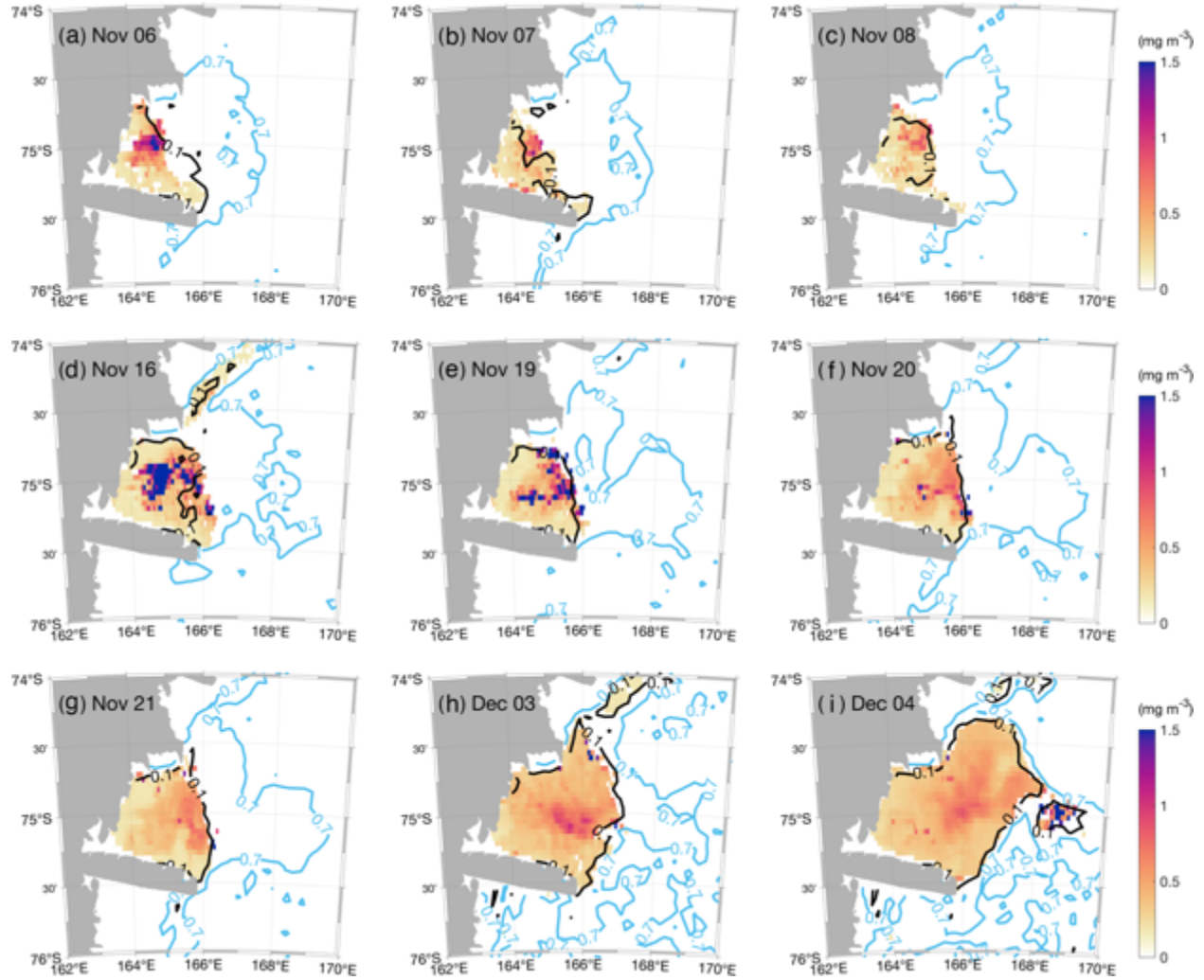


**Fig. 4.** Snapshots of chlorophyll-a concentration (color) and sea ice concentration (contours) in the Terra Nova Bay Polynya in November and December, 2019. The black contours indicate 10% sea ice concentration, and the blue contours denote 70% sea ice concentration. The coastline is obtained from the GSHHG data set (Wessel & Smith, 1996).

## 2. Method

### 2.1. Model Configuration

A coupled ice-shelf/sea-ice/ocean numerical model is used to simulate an idealized coastal polynya. The model is adapted from the MIT General Circulation Model (MITgcm; Losch, 2008; Marshall et al., 1997) and designed to qualitatively reproduce the configuration of the TNBP with the orientation rotated by  $90^\circ$  counterclockwise. A comprehensive description of the model configuration is provided in Xu et al. (2023a; 2023b). The model covers a geographical extent of 22.5 degrees longitude and 6 degrees latitude (Fig. 4). Its horizontal grid spacing is  $\sim 1$  km in the polynya region adjacent to the ice shelf and gradually expands towards the boundaries. The vertical grid spacing is 10 m uniformly. The domain has a flat seafloor of 500 m depth and a floating ice shelf protruding southward into the continent. An ice tongue is positioned to the immediate east of the polynya and ice shelf opening, exhibiting a three-dimensional shape that qualitatively mimics the Drygalski Ice Tongue (Stevens et al., 2017). The ice tongue spans 111 km (1 degree in latitude) in the cross-shore direction and 28 km wide in the alongshore direction. The ice tongue draft decreases gradually from 400 m at the coast to 0 m at the offshore end. Moreover, a headland is added to the west of the ice shelf opening to mimic the coastal geometry around Cape Washington. A coastal polynya is formed in the model by an offshore-blowing wind at the center of the domain with a speed of  $V_{wind} = V_a[1 - \cos(2\pi t/P_{wind})]$ , where  $t$  is time,  $V_a$  is the mean wind speed, and  $P_{wind} = 2$  days is the wind oscillation period. To capture the bifurcation of the katabatic wind around the Drygalski Ice Tongue as produced by the Antarctic Mesoscale Prediction System (AMPS; Powers et al., 2012; Fig. 2c), another offshore wind with a speed of  $V_{wind}/2$  is added to the immediate east of the ice tongue in the model. Adding this additional offshore wind gives a better match of modeled sea ice distribution on the east side of the ice tongue to the satellite observation (Fig. 1), but it does not affect the result of this study on the polynya restratification. To mimic the along-shore wind in the TNBP region (consistent with the prominent coastal easterly in other Antarctic coastal regions), a steady westward downwelling-favorable alongshore wind, with a speed of  $U_a$ , is applied in the model. The alongshore wind extends across the entire study region and diminishes linearly within an 80–110 km boundary ramping zone to 0 on the open boundaries. To mitigate boundary condition issues related to sea ice, sea ice

concentration and thickness are set to 0 at all open boundaries. Meanwhile, the Orlanski radiation condition (Orlanski, 1976) is used for other state variables on the open ocean boundaries.

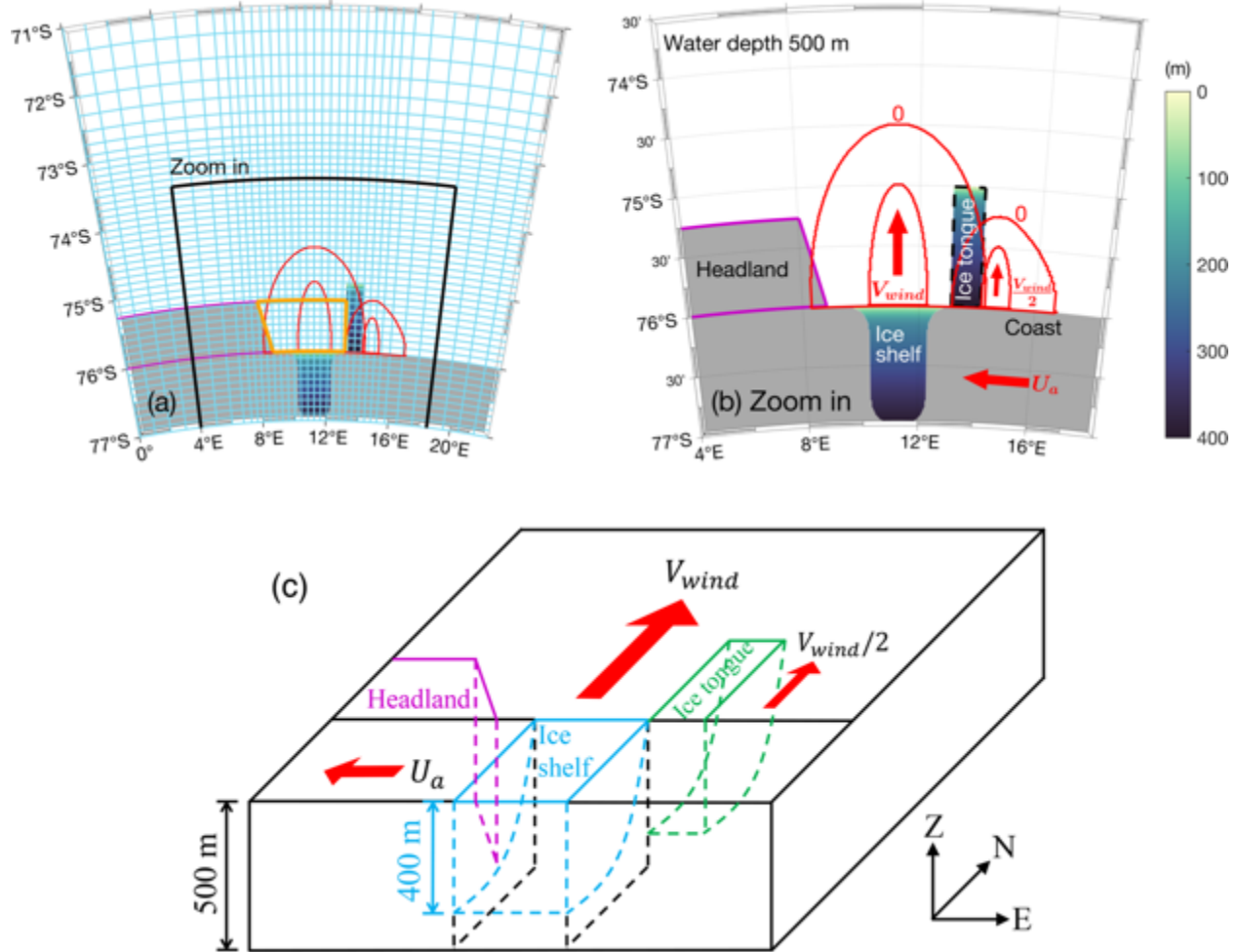


**Fig. 5.** Model configurations: (a) an aerial view of the model domain, with every 10 horizontal grid cells marked by blue lines and land areas shown in grey. The filled color represents the vertical position of the ice-ocean interface, which is equivalent to the thickness of the ice shelf/tongue in the model. Areas of the offshore katabatic wind  $V_{wind}$  and its inner region of maximum speed are denoted in the red ellipses. Orange lines denote the polynya region used for calculations in Section 3. (b) A detailed view of the area outlined in the black frame in (a), with the  $V_{wind}$  and the alongshore easterly winds,  $U_a$  indicated by red arrows. The shape of the headland is traced by purple lines, and the shape of the ice tongue is marked by the black dashed frame. (c) A three-dimensional schematic of the model setup.

224

225       To provide the initial condition for the spring simulations, a 150-day winter simulation  
226 similar to those in Xu et al. (2023a; 2023b) is carried out first. In the winter simulation,  $V_a = 20$   
227  $\text{m s}^{-1}$ ,  $U_a = 10 \text{ m s}^{-1}$ , air temperature remains constant at  $-20^\circ\text{C}$ , downward longwave radiation is  
228 steady at  $200 \text{ W m}^{-2}$ , and downward shortwave radiation is 0. On Day 150, the winter simulation  
229 produces a coastal polynya in the center of the domain and immediately offshore of the ice shelf  
230 (Fig. 6a). The winds push sea ice moving offshore forming a sea ice plume (Fig. 6b), resembling  
231 the satellite observation in Fig. 1a. Meanwhile, high-density water, formed at the polynya surface,  
232 has mixed down to the bottom and occupies the entire polynya water column (Fig. 6c-d). There is  
233 thus no stratification in the polynya water column in the initial condition of the subsequent spring  
234 simulation.

235       Most of the spring simulations span 100 days (Day 150–250). Their atmospheric forcing  
236 is designed to qualitatively capture observed temporal variation (Fig. 2a-b) and AMPS-modeled  
237 spatial variation (Powers et al., 2012; Fig. 2c) in the atmospheric condition in the TNBP region.  
238 Based on measurements from Automatic Weather Stations (Fig. 2) and the ERA5 reanalysis  
239 product (Hersbach et al., 2020), in the Base Run A1, the air temperature rises steadily from  $-20^\circ\text{C}$   
240 on Day 150 to  $-5^\circ\text{C}$  on Day 250, while downward longwave radiation increases from  $200 \text{ W m}^{-2}$   
241 to  $250 \text{ W m}^{-2}$  and shortwave radiation increases from 0 to  $400 \text{ W m}^{-2}$  over the same period. The  
242 westward alongshore wind,  $U_a$ , remains constant at  $4 \text{ m s}^{-1}$ , while the mean cross-shore wind,  $V_a$ ,  
243 gradually weakens from  $20 \text{ m s}^{-1}$  to  $5 \text{ m s}^{-1}$  over the period. After Day 250, all these parameters  
244 maintain their values on Day 250. Sensitivity simulations with altered parameter values are carried  
245 out in this study (Table 1). Note that, in each sensitivity simulation, only the value of one parameter  
246 is altered from the Base Run A1.

247       To examine the influence of the ice shelf basal meltwater on the polynya restratification, it  
248 is necessary to alter the basal melt rate in the model. In the ocean, the basal melt rate is controlled  
249 by the volume and temperature of the intruding CDW. Because the idealized simulations in this  
250 study do not have CDW intrusion, we choose to directly modify water temperature in the modeled  
251 ice shelf cavity (below 250 m and south of  $76.3^\circ\text{S}$ ). In each of the sensitivity simulations, S-  
252 CWTemp, water temperature inside the ice shelf cavity is fixed to a value between  $-1.8$  and  $-1.5^\circ\text{C}$ ,  
253 all slightly above the freezing point of around  $-1.9^\circ\text{C}$ . This temperature range of the cavity water

is based on available in situ observations from the cavity of the Ross Ice Shelf (Malyarenko et al., 2019), as well as subsurface (below 250 m) measurements in the TNBP gathered by instrumented seals (Fig. 3a) and hydrographic surveys (e.g., Rusciano et al., 2013). Analysis of our sensitivity simulations show that this simple approach of modifying the water temperature in the ice shelf cavity captures the first-order influence of the ice shelf basal meltwater on restratification in the upper part of the polynya water column (see below). In the Base Run A1, the water temperature in the ice shelf cavity is fixed at -1.8 °C.

**Table 1.** Parameter values in the Base Run A1 and sensitivity simulation sets. The altered values of the parameters are shown in bold. Bracket denotes the range of the parameter values.

Sensitivity simulation set	Along-shore wind speed $U_a$ ( $\text{m s}^{-1}$ )	Off-shore wind speed $V_a$ on Day 250 ( $\text{m s}^{-1}$ )	Air temperature $T_a$ on Day 250 ( $^{\circ}\text{C}$ )	Cavity water temperature $T_{cavity}$ ( $^{\circ}\text{C}$ )	Longwave radiation on Day 250 ( $\text{W m}^{-2}$ )	Shortwave radiation on Day 250 ( $\text{W m}^{-2}$ )	Surface runoff period $P_r$ (days)
A1	4	5	-5	-1.8	250	400	0
S-AWind	<b>[0, 10]</b>	5	-5	-1.8	250	400	0
S-OWind	4	<b>10</b>	-5	-1.8	250	400	0
S-ATemp	4	5	<b>[-10, 0]</b>	-1.8	250	400	0
S-CWTemp	4	5	-5	<b>[-1.8, -1.5]</b>	250	400	0
S-LWRad	4	5	-5	-1.8	<b>[200, 300]</b>	400	0
S-SWRad	4	5	-5	-1.8	250	<b>[350, 450]</b>	0
S-SRunoff	4	5	-5	-1.8	250	400	<b>[0, 90]</b>

Few observations of the surface runoff of glacial surface meltwater exist, and the runoff rate and its temporal and spatial variability are poorly constrained in the literature (Bell et al., 2017; Bell et al., 2018). Nevertheless, to provide a qualitative understanding of the potential influence of the surface runoff on the polynya restratification, sensitivity simulations, S-SRunoff, with prescribed surface runoff are carried out. The values of the surface runoff are prescribed based on

an estimate by Bell et al. (2017). The Nansen Ice Shelf has an area of about 1800 km<sup>2</sup>, and analyses suggest that the surface melt erodes ~0.05–0.5 m of ice annually (Bell et al., 2017; Bell et al., 2018). We assume that the upper-bound of the estimated ice shelf surface meltwater in a year, i.e., 0.5 m, is entirely injected into the ocean surface immediately offshore of the ice shelf front in the end of the spring simulation over a period of  $P_r$ , and the injection occurs uniformly along the ice shelf front in a steady rate. Therefore, a total surface runoff injection of  $9 \times 10^8$  m<sup>3</sup> freshwater is added to the model over the period of Day (250- $P_r$ ) to 250. The value of  $P_r$  changes in the range of 0–90 days among the S-SRunoff sensitivity simulations. In the Base Run A1,  $P_r = 0$ , and the surface runoff is not considered.

To compare the distribution of sea ice meltwater, ice shelf basal meltwater, and surface runoff, three passive tracers, corresponding to the three types of meltwaters, are implemented in the model. Passive tracer concentrations have initial values of 0 everywhere. During the simulations, they are assigned to be 1 in every 1 m<sup>3</sup> of the corresponding meltwater that is injected into the ocean at the interface. The passive tracers then evolve with the modeled 3-dimensional ocean circulation, providing a way to show the volume concentration of the meltwaters and quantitatively compare contributions of the meltwaters to restratification of the upper water column in the polynya region.

## 2.2. Restratification Intensity

To quantify the stratification intensity in the polynyas, we compute vertically-integrated potential energy anomaly,  $\phi$ , in the upper part of the polynya water column following Simpson et al. (1990),

$$\phi = \int_{-h}^0 (\bar{\rho} - \rho) g z dz. \quad (1)$$

Here,  $z$  is the vertical coordinate,  $h$  is the thickness of the upper water column of interest,  $g$  is gravitational acceleration,  $\rho$  is the water density,  $\bar{\rho} = \frac{1}{h} \int_{-h}^0 \rho dz$  is the vertically-averaged density in the polynya upper water column of interest. Essentially,  $\phi$  describes the amount of energy required to completely mix water in the upper part ( $[-h, 0]$ ) of the water column. A greater  $\phi$  indicates stronger stratification in the depth range of  $[-h, 0]$ . The area-integrated potential energy anomaly  $\Phi_p$  in a polynya with surface area  $S$  is therefore,



299

$$\Phi_p = \iint_S \phi dS. \quad (2)$$

300

301

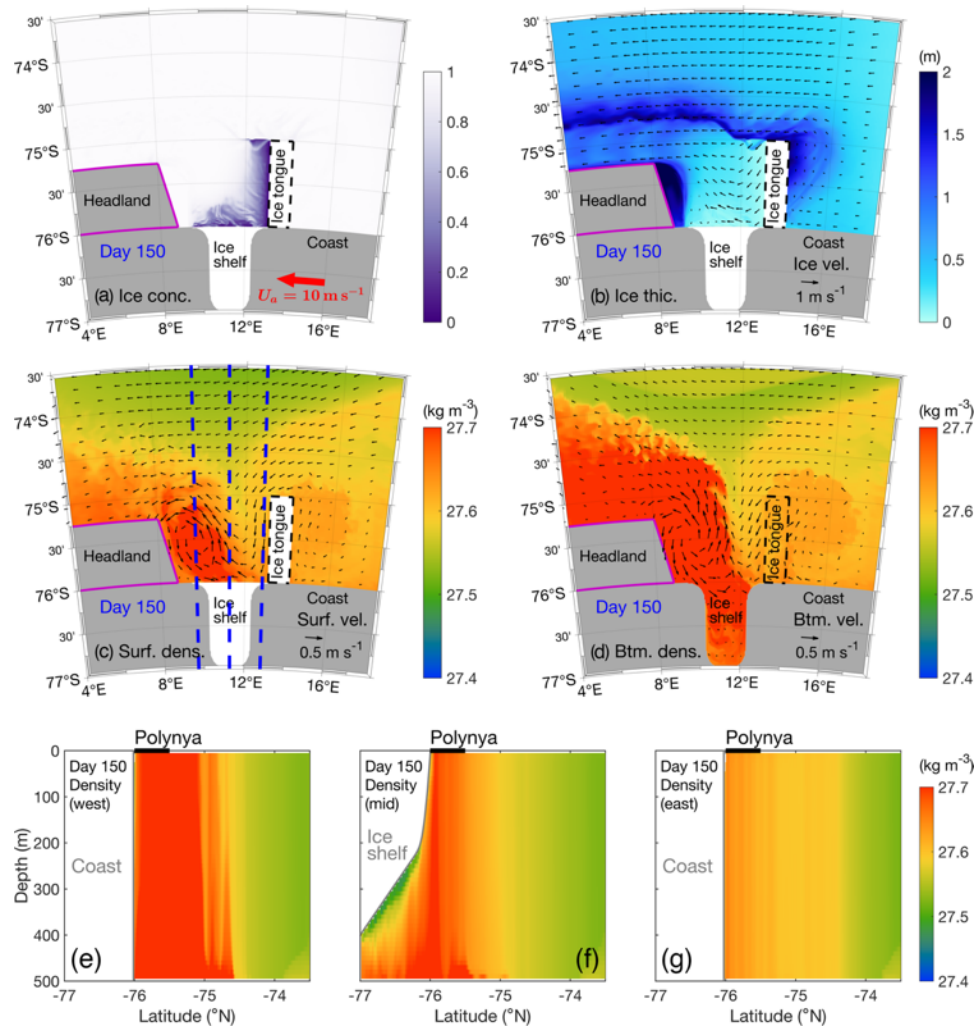
302

303

304

305

In this study, the polynya area changes with time as the sea ice undergoes melting in spring. To ensure a fair comparison, we define the polynya area as the fixed region enclosed by the ice tongue, ice shelf front and headland (Fig. 5a). Because this study is motivated by understanding the dynamics of phytoplankton blooms in the coastal polynyas and the phytoplankton bloom occurs mostly in the top 100 m of the water column (Long et al., 2012),  $h$  is set to 100 m.



306

307

308

309

**Fig. 6.** Snapshots of the model fields at the end of the winter simulation on Day 150, which serves as the initial condition of the spring simulation: (a) sea ice concentration; (b) sea ice thickness (color) and velocity (arrows); potential density (color) and velocity (arrows) at the (c)

surface and (d) bottom. The blue dashed lines in (c) delineate the locations of three cross-shore transects of potential density in the western end (e), middle (f), and eastern end (g) of the polynya.

### 3. Results

#### 3.1. Modeled Restratification Pattern

In this section, we elucidate the general pattern of modeled springtime polynya restratification by examining result of Base Run A1 on Days 210, 230, and 250 (Figs. 7 and 8), representative of roughly 2, 2.5, and 3.5 months after the onset of springtime simulation (Day 150). During this period, the offshore wind has weakened, surface heating increased, and sea ice started to melt. As surface heating intensifies, sea ice starts to melt in the polynya region (Fig. 7). Driven by both offshore and alongshore winds, the polynya opening expands towards the northwest. Meanwhile, the alongshore wind pushes the pack sea ice offshore of the ice tongue, and the pack ice then moves westward and passes through the region north of the polynya. In the region to the immediate east of the ice tongue, owing to the ice tongue blocking the westward flow, modeled sea ice had accumulated with a thickness greater than 1 m (Fig. 6). This pattern is similar to the observed land-fast ice to the east of Drygalski Ice Tongue (Fig. 1a). Starting on Day 210, the accumulated sea ice in the model begins to dislodge. The detached sea ice is subsequently propelled offshore by the offshore winds, merging with the existing offshore sea ice and flowing westward. In contrast, on the eastern side of the headland, the accumulated sea ice remains relatively stable with limited movement after Day 210. This is likely caused by its considerably higher initial thickness ( $> 2$  m) at the end of the wintertime simulation (Fig. 6b). Overall, although the modeled sea ice thickness offshore of the polynya is slightly thinner than the observed (Kacimi & Kwok, 2020; Rack et al., 2020), a likely consequence of no transport of sea ice into the model domain across the open boundaries, the evolution of the modeled sea ice field (Fig. 7) qualitatively matches that described by the satellite observations (Fig. 1b-g).

The model also shows gradual development of the near-surface stratification within the polynya region as well as the neighboring region offshore. After Day 210, as sea ice melts, the surface density decreases (Fig. 8a-c), and vertically-integrated potential energy anomaly,  $\phi$ , within the upper 100 m of the water column increases (Fig. 8d-f). Note that, in the initial condition (at the end of the wintertime simulation), surface density in the polynya region is higher than the offshore

region due to preeminent dense water formation in the polynya (Fig. 6c). In the spring simulation, while both the polynya and offshore regions undergo water column restratification, they differ considerably in timing and intensity. The offshore area experiences earlier restratification with much lower surface density (Fig. 8c). This is consistent with the modeled sea ice field showing the offshore region containing more sea ice than the polynya region (Fig. 7), which presumably leads to more localized sea ice melting and surface freshwater (i.e., buoyancy) input in the offshore region.

Surface concentrations of both sea ice meltwater and ice shelf basal meltwater passive tracers reveal a notable heterogeneity in their horizontal distribution (Fig. 8g-l). This pattern is consistent with modeled variation in surface density and potential energy anomaly. For instance, a high concentration of sea ice meltwater is initially found in the offshore openings where sea ice melts first. The peak concentration gradually spreads to the surrounding regions as the sea ice continues to melt. Note that there is little sea ice meltwater from the polynya itself because sea ice there has been transported offshore by the offshore winds. Consequently, the sea ice meltwater in the polynya area originates from the offshore region and is transported into the polynya area by the surface current. Conversely, the ice shelf basal meltwater (Fig. 8j-l) is concentrated in the polynya area. Meltwater from the ice shelf base ascends in the ice shelf cavity and then reaches the polynya surface where it exhibits a high concentration towards the west end of the polynya. The westward flow of the ice shelf basal meltwater is presumably caused by the Coriolis force turning the offshore outflow leftward, consistent with outflows of ice shelf basal meltwater along the western boundaries of ice shelf cavities identified in other studies (e.g., Galton-Fenzi et al., 2012). Moreover, the injection of the ice shelf basal meltwater into the polynya water column in our model is steadier over time than the sea ice meltwater. This is because the ice shelf basal melt in the model is induced by the prescribed constant water temperature in the ice shelf cavity.

Development of the stratification in the polynya also exhibits spatial inhomogeneity, as indicated by cross-shore sections of density, sea ice meltwater, and ice shelf basal meltwater (Fig. 9). On Day 250, the west end of the polynya has the lowest surface density and the strongest near-surface stratification, whereas the east end remains largely unstratified (Fig. 9a-c). This pattern is consistent with concentration of both sea ice meltwater (Fig. 9d) and ice shelf basal meltwater (Fig. 9g) at the west end of the polynya. Vertical density profiles on the west end of the polynya show two layers of gradient, one at about 200 m depth, and the other at about 30 m depth. The former

correspond to the vertical extent of the ice shelf basal meltwater (Fig. 9g), and the latter to the shallower lens of sea ice meltwater on the surface (Fig. 9d). This modeled two-layer stratification in the polynya qualitatively resemble the density profiles captured by the instrumented seals (Fig. 3). These complexities and heterogeneity in meltwater distribution underscore the need for a holistic investigation of the causes, which will be the goal of the following sections.

## **3.2. Influences on Sea Ice Meltwater Distribution**

### **3.2.1. Roles of Alongshore Winds**

To examine the influence of the predominantly downwelling-favorable alongshore winds on the dispersal of sea ice meltwater, sensitivity simulations, we carry out the S-AWind experiment by varying the alongshore wind speed of the Base Run A1 from 0 to  $10 \text{ m s}^{-1}$ , are carried out. Time evolution of the amount of area-integrated sea ice meltwater passive tracer (Fig. 10a), ice shelf basal meltwater passive tracer (Fig. 10b), and the potential energy anomaly (Fig. 10c) within the upper 100 m of the polynya water column are calculated. As the speed of the alongshore wind rises, the amount of sea ice meltwater within the polynya water column diminishes. This is caused by alongshore wind pushing offshore sea ice away from the offshore region, leading to less meltwater being transported to the polynya area by the currents. This effect is highlighted in Fig. 11 and Fig. 12. When the alongshore wind speed is set to 0, sea ice melts mostly locally in both the polynya and the immediate offshore region (Fig. 11), instead of being carried westward by alongshore winds (Fig. 7). Having the alongshore wind speed at 0 leads to a significantly increased surface concentration of sea ice meltwater, reduced surface density (Fig. 12a-c), and enhanced potential energy anomaly (Fig. 12d-f) in the polynya area compared to the results in Run A1 (Fig. 8). A more detailed comparison of vertical profiles of horizontally integrated passive tracers of sea ice meltwater in the polynya area (Fig. 13) reveals that, without alongshore wind, a notably higher concentration of sea ice meltwater exists within the top 50 m of the polynya water column than when the alongshore wind speed is  $4 \text{ m s}^{-1}$  (Base Run A1). Note that the amount of ice shelf basal meltwater in the polynya area exhibits less sensitivity to changes in alongshore wind speed (Figs. 10b, 13a-b), because the ice shelf basal meltwater rises from the deep and is less subject to the influence of surface forcings.

### 3.2.2. Roles of Offshore Winds

Offshore winds in the polynya region weakens from winter to spring (Fig. 2b), and the average offshore wind speed during the spring season is about  $5 \text{ m s}^{-1}$ . This offshore wind could potentially mix the freshwater layer at the surface and enhance the mixing in the water column. To evaluate the influences of offshore winds on the distribution of meltwater, we increase the mean offshore wind speed from  $5 \text{ m s}^{-1}$  in the Base Run A1 to  $10 \text{ m s}^{-1}$  in a sensitivity simulation, S-OWind. The comparison between this new case and A1 shows that the increase of offshore wind speed,  $V_a$ , does not dramatically change the amount of sea ice meltwater in the entire polynya water column (Fig. 14c), but greatly reduces potential energy anomaly and thus near-surface stratification in the polynya area (Fig. 14d). This change of near-surface stratification results from vertical mixing of sea ice meltwater in the upper water column induced by the offshore winds. With enhanced offshore winds, the sea ice meltwater is mixed deeper into the polynya water column than that in A1 (Fig. 13c). Consistently, with the increase of  $V_a$  from  $5$  to  $10 \text{ m s}^{-1}$ , the surface boundary layer depth in the polynya area averaged between Day 240 and 250 increases from  $10\text{--}40 \text{ m}$  to  $50\text{--}150 \text{ m}$  (Fig. 15). Here, the surface boundary layer depth is determined using a critical bulk Richardson number of 0.3. This result further confirms that the offshore wind speed can vertically mix the sea ice meltwater and suppress stratification in the upper water column of the polynya.

### 3.2.3. Thermodynamic Effects

Another potential factor influencing restratification in polynyas is the surface heat flux, which could modulate sea ice melt rate and affect the amount of sea ice meltwater being injected into the polynya area. To assess this thermodynamic effect, we carried out additional simulations with modified peak values of longwave and shortwave radiations and air temperature. In the S-LWRad (S-SWRad) simulations, the peak longwave (shortwave) radiation in the end of the spring is set at  $200$  and  $300 \text{ W m}^{-2}$  ( $350$  and  $450 \text{ W m}^{-2}$ ), that is,  $50 \text{ W m}^{-2}$  lower and higher than the control values in the Base Run A1, respectively. In the S-ATemp simulations, the peak air temperature in the end of the spring is set at  $0^\circ\text{C}$  and  $-10^\circ\text{C}$ ,  $5^\circ\text{C}$  higher and lower than the default value of  $-5^\circ\text{C}$  in the Base Run A1, respectively. Temporal evolution of modeled sea ice meltwater passive tracer and the potential energy anomaly in the polynya area under these altered conditions

reveal that an increase in heat input to the polynya surface substantially increases both the concentration of sea ice meltwater and the strength of newly developed stratification in the polynya area (Fig. 14a-d). Detailed examination of the model solutions indicates that this indeed results from surface heat flux affecting the amount of sea ice being melted in the region surrounding the polynya and then the amount of sea ice melt flows into the polynya area. With increased surface heat flux, sea ice is melted more quickly in the local region, and less sea ice being carried away by the winds.

It is worth noting that increasing longwave/shortwave radiations by  $50 \text{ W m}^{-2}$  and elevating air temperature by  $5 \text{ }^{\circ}\text{C}$  have a similar influence on sea ice melt and potential energy anomaly. This similarity can be explained by calculating the change in sensible heat flux induced by the air temperature change,

$$Q_s = \rho_a C_h C_p V_a (T_a - T_w), \quad (3)$$

where  $\rho_a = 1.3 \text{ kg m}^{-3}$  is the air density,  $C_h = 0.002$  is the heat transfer coefficient,  $C_p = 1004 \text{ J }^{\circ}\text{C}^{-1} \text{ kg}^{-1}$  is the specific heat of air,  $T_a$  is air temperature, and  $T_w$  is the temperature of the surface water. For an air temperature difference of  $5 \text{ }^{\circ}\text{C}$ , the difference in  $Q_s$  is about  $65 \text{ W m}^{-2}$ , similar to the  $50 \text{ W m}^{-2}$  prescribed change in longwave or shortwave radiation.

### 3.3. Influences of Ice Shelf Basal Melt

In this section, we examine the sensitivity simulations, S-CWTemp, with altered water temperatures within the ice shelf cavity,  $T_{cavity}$ , to explore the impact of ice shelf basal melt on the polynya near-surface restratification. As  $T_{cavity}$  increases, the amount of ice shelf meltwater within the top 100 m of the polynya water column increase dramatically (Fig. 10e). However, the area-integrated potential energy anomaly in the 100 m of the polynya water column does not vary as much (Fig. 10f). This suggests that the influence of ice shelf basal meltwater on the near-surface restratification in the polynya area is relatively weak. A plausible explanation for this lies in the considerable mixing that ice shelf basal meltwater undergoes with the surrounding ambient water as it ascends in the buoyant plume from the subsurface. This mixing process disperses the ice shelf basal meltwater throughout the upper part of water column, which diminishes its impact on near-

surface stratification. This stands in contrast to sea ice meltwater, which is directly injected onto the polynya surface and therefore exerts a stronger influence on the near-surface stratification.

Here we combine numerical and analytical approaches to assess the vertical length scale of the buoyant plume associated with ice shelf basal meltwater as it moves toward the surface of the polynya. First, from the vertical profile of the ice shelf basal meltwater passive tracer horizontally integrated in the polynya area in Base Run A1 (the red line in Fig. 13a), using an e-folding length scale, we determine the vertical length scale of the buoyant outflow plume of the ice shelf basal meltwater is about 180 m. This means the modeled ice shelf basal meltwater is mixed in the top 180 m once it exits the cavity and flow into the polynya area. The vertical length scale of the buoyant outflow plume can also be estimated through an analytical buoyant plume theory. Fig. 16 illustrates a schematic representation of a buoyant plume at the ice shelf front, following Wang et al. (2023). In this study, the ice shelf meltwater flows out of the cavity over a region of  $\sim 10$  km width in the zonal direction at the western end of the polynya. It ascends almost vertically along the ice shelf front wall after passing by the ice shelf bend (Fig. 16a), forming a buoyant plume (as indicated in Figs. 8l, 9i). The buoyant plume ascends to the surface at a vertical speed of  $W_p$  before turning offshore forming a horizontal flow of less dense water at the surface with the thickness of  $D_0$  and a speed of  $U_0$ . Using the estimated thickness of 180 m, we obtain the bulk Richardson number of the plume outflow  $Ri = \frac{\Delta\rho g D_0}{\rho_0 \Delta V^2} \approx 69$ , where  $\Delta\rho = 0.1 \text{ kg m}^{-3}$ ,  $\Delta V = 0.05 \text{ m s}^{-1}$  are the density difference and velocity difference between the plume and the layer below, respectively,  $g$  is gravitational acceleration,  $\rho_0 = 1027 \text{ kg m}^{-3}$  is the reference density. With  $Ri > 6$ , following Ching et al. (1993) and Wang et al. (2023), we have an approximate relationship between  $U_0$  and  $W_p$ ,

$$U_0 = 0.95W_p. \quad (4)$$

Assuming the buoyant plume is a line source, following Linden et al. (1990),  $W_p$  can be expressed as,

$$W_p = (2\alpha)^{-\frac{1}{3}}(B/l_0)^{\frac{1}{3}}, \quad (5)$$

where  $\alpha = 0.13$  is the entrainment rate between the plume and ambient water,  $l_0$  is the alongshore width of the plume,  $B = g'Q_i$  is the plume buoyant flux,  $Q_i$  is the plume volume flux at the ice



shelf bend,  $g' = g(\rho_p - \rho_{aw})/\rho_0$  is the reduced gravity,  $\rho_p$  is the plume density,  $\rho_{aw}$  is the density of ambient water.

For a line-source plume, following Linden et al. (1990), the volume flux of the near-surface plume outflow in the offshore direction,  $Q_0$ , is,

$$Q_0 = (2\alpha)^{\frac{2}{3}}(B/l_0)^{\frac{1}{3}}D_i l_0 = (2\alpha)^{\frac{2}{3}}(g' Q_i / l_0)^{\frac{1}{3}}D_i l_0, \quad (6)$$

where  $D_i$  is the depth of the ice shelf. Combining (4), (5), (6), and the volume conservation equation in the surface layer,

$$Q_0 = U_0 l_0 D_0, \quad (7)$$

we obtain an expression for the vertical length scale of the buoyant plume,  $D_0$ ,

$$D_0 = \frac{2\alpha D_i}{0.95}. \quad (8)$$

Equation (8) shows that, in the configuration of the interest of this study, the vertical length scale of the buoyant outflow plume at the polynya surface mainly depends on the depth of the ice shelf. In our Base Run A1, the depth of the ice shelf,  $D_i$ , is 400 m, and thus  $D_0$  is about 110 m. This magnitude is qualitatively consistent with the modeled vertical length scale of the horizontal outflow plume.

To further validate the scaling analysis, we qualitatively compare the modeled and scaled horizontal plume outflow speed. Model diagnostics show that the average freshwater flux from the ice shelf basal melt is  $Q_f = 350 \text{ m}^3 \text{ s}^{-1}$ . Within the ice-ocean boundary layer below the ice shelf, the salinity is  $S_i = 34.1$  psu, while the ambient salinity is  $S_a = 34.3$  psu. Using salt conservation, we obtain the plume volume flux at the ice shelf bend  $Q_i = Q_f S_a / (S_a - S_i) \approx 6 \times 10^4 \text{ m}^3 \text{ s}^{-1}$ . Applying the model result,  $g' = 0.002 \text{ m s}^{-2}$  and  $l_0 = 10 \text{ km}$ , to (4) and (5), we obtain  $U_0 \approx 0.34 \text{ m s}^{-1}$ . The magnitude of this analytically derived offshore outflow speed of the plume is consistent with the outflow velocity in the model.

Therefore, both the numerical and analytical results indicate that extensive mixing of the ice shelf basal meltwater with the ambient water during the ascent of the meltwater causes the basal meltwater to be distributed in a surface layer with a thickness of more than 100 m. This explains that the ice shelf basal meltwater has a weak influence on the potential energy anomaly in the top 100 m of the polynya water column and does not contribute much to the biologically

important *near-surface* restratification, despite that it delivers a substantial amount of freshwater into the polynya water column and enhances stratification over the entire polynya water column.

### 3.4. Influences of Surface Runoff

In this section, we investigate the impact of surface runoff of the ice shelf surface melt on the polynya restratification, and the S-SRunoff simulation with a runoff duration  $P_r = 30$  days in the end of the spring simulation is used first as an example to describe the general pattern (Fig. 17). The simulation shows that the released runoff water flows westward and accumulate near the coast of the headland (Fig. 17c), driven by the Coriolis force. This spatial distribution of the runoff water in the polynya area aligns with the low surface density and elevated potential energy anomaly near the headland (Fig. 17a-b).

Vertically, the surface runoff water is mainly confined in the very top of the water column, as both evidenced by the runoff water passive tracer vertical profile horizontally integrated in the polynya (Fig. 13d) and the cross-shore section of the runoff water passive tracer (Fig. 17g). This vertical distribution closely resembles that of sea ice meltwater. However, on the horizontal plane, surface runoff water is primarily situated nearshore within the polynya, different from the mostly offshore presence of sea ice meltwater. Overall, adding the surface runoff greatly modifies near-surface stratification in part of the polynya region. Note that the runoff meltwater released in this study represents an upper limit of the estimated ice shelf surface melt (Bell et al., 2017; Bell et al., 2018). The exact influence of the runoff on the restratification in an Antarctic coastal polynya region depends on the overall amount of ice shelf surface melt and also the rate of the melt, the latter of which is considered in this study by changing the duration of the runoff release.

To investigate the impact of the rate of the runoff release, we examine other S-SRunoff simulations with  $P_r = 10$  and 90 days (Fig. 14e-f). Here, the total runoff volume is kept the same while  $P_r$  is altered. The simulations show that a decrease in  $P_r$ , i.e., an increase in runoff rate over the release period, generally correlates with an increase in potential energy anomaly in the polynya region. However, when  $P_r = 10$  or 30 days, the changes in the final amount of runoff meltwater and potential energy anomaly in the polynya area are relatively small. This results from the residence time of the runoff meltwater in the polynya region being longer than 30 days. When the release period is equal or less than 30 days, most of the runoff water remains in the polynya region,

and the duration of the release has little influence on the overall polynya restratification. When  $P_r$  increases to 90 days, which is longer than the residence time of the runoff water in the polynya region, some of the runoff water exits the polynya region. Correspondingly, the potential energy anomaly within the polynya area decreases.

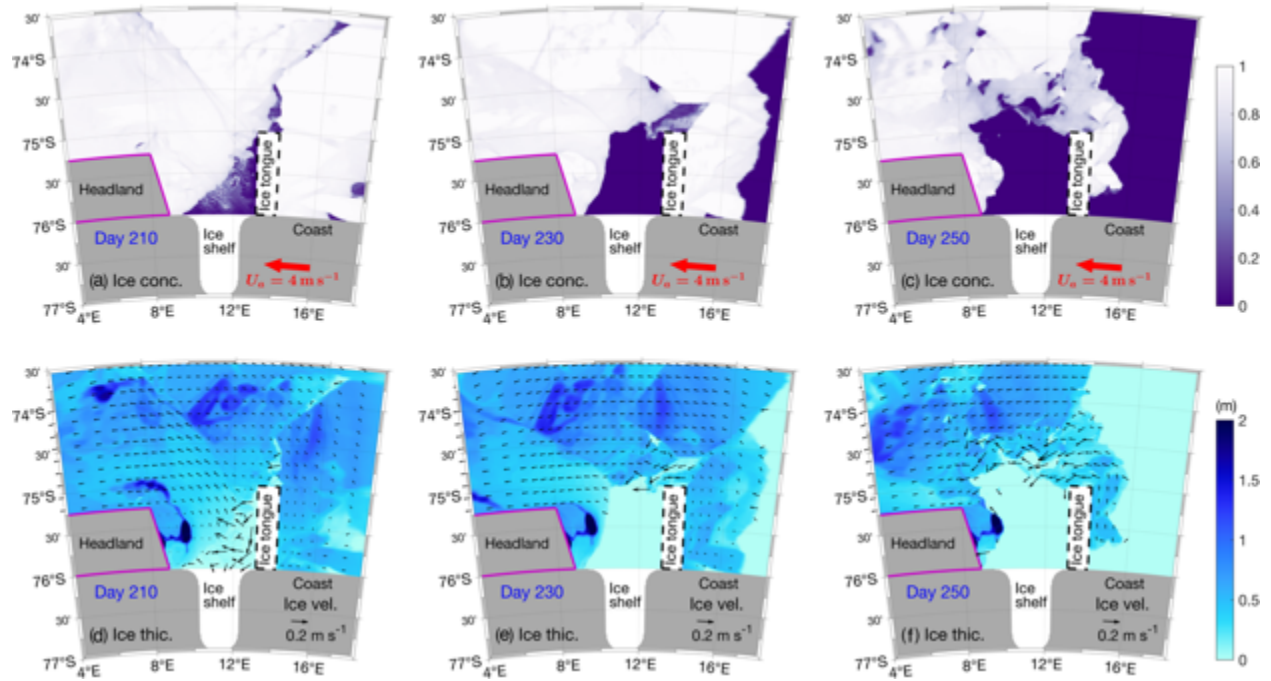


**Fig. 7.** Base Run A1: snapshots of the modeled (a-c) sea ice concentration; (b-d) sea ice thickness (color) and sea ice velocity (arrows) on Days 210 (left), 230 (middle), and 250 (right).

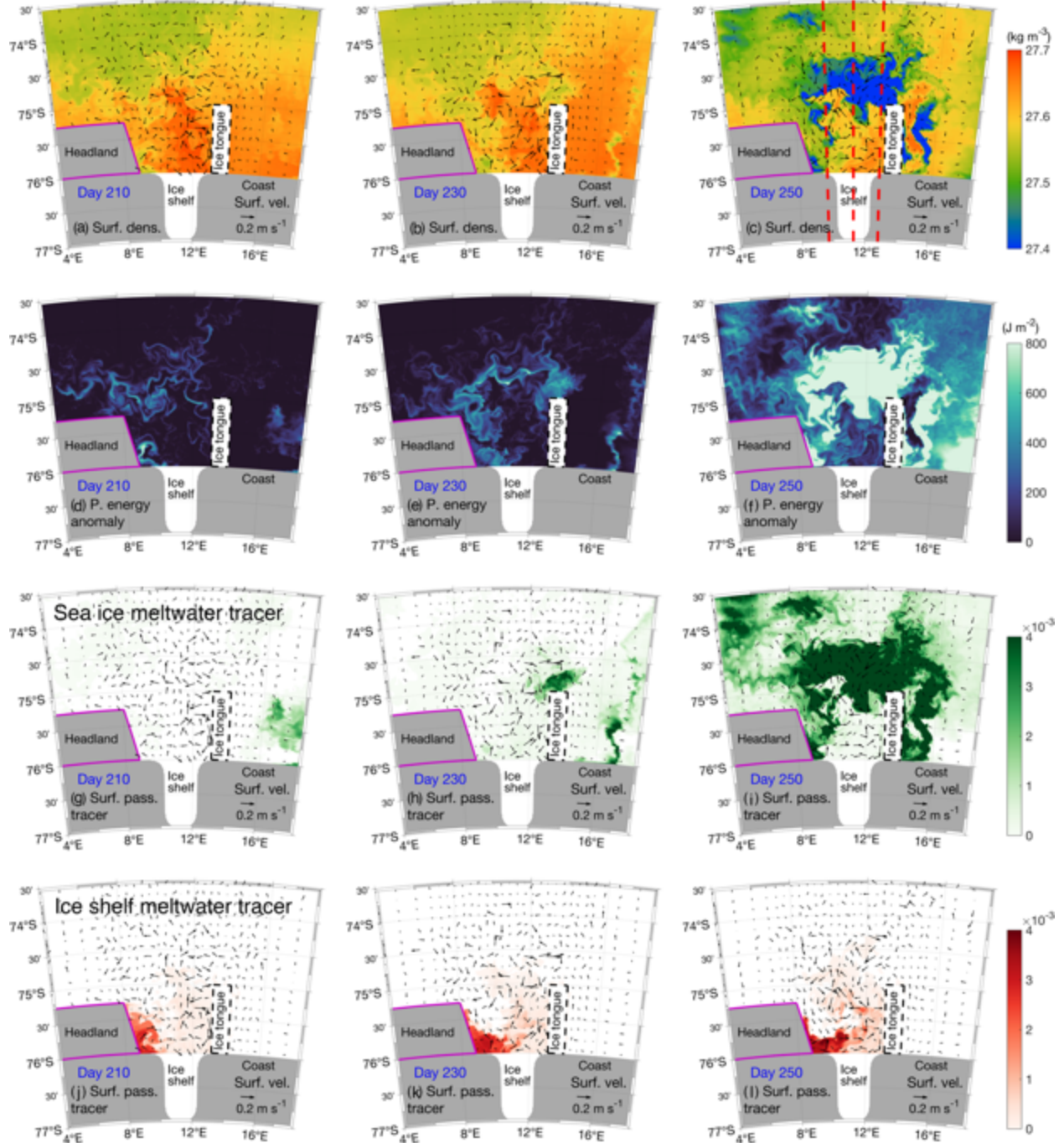
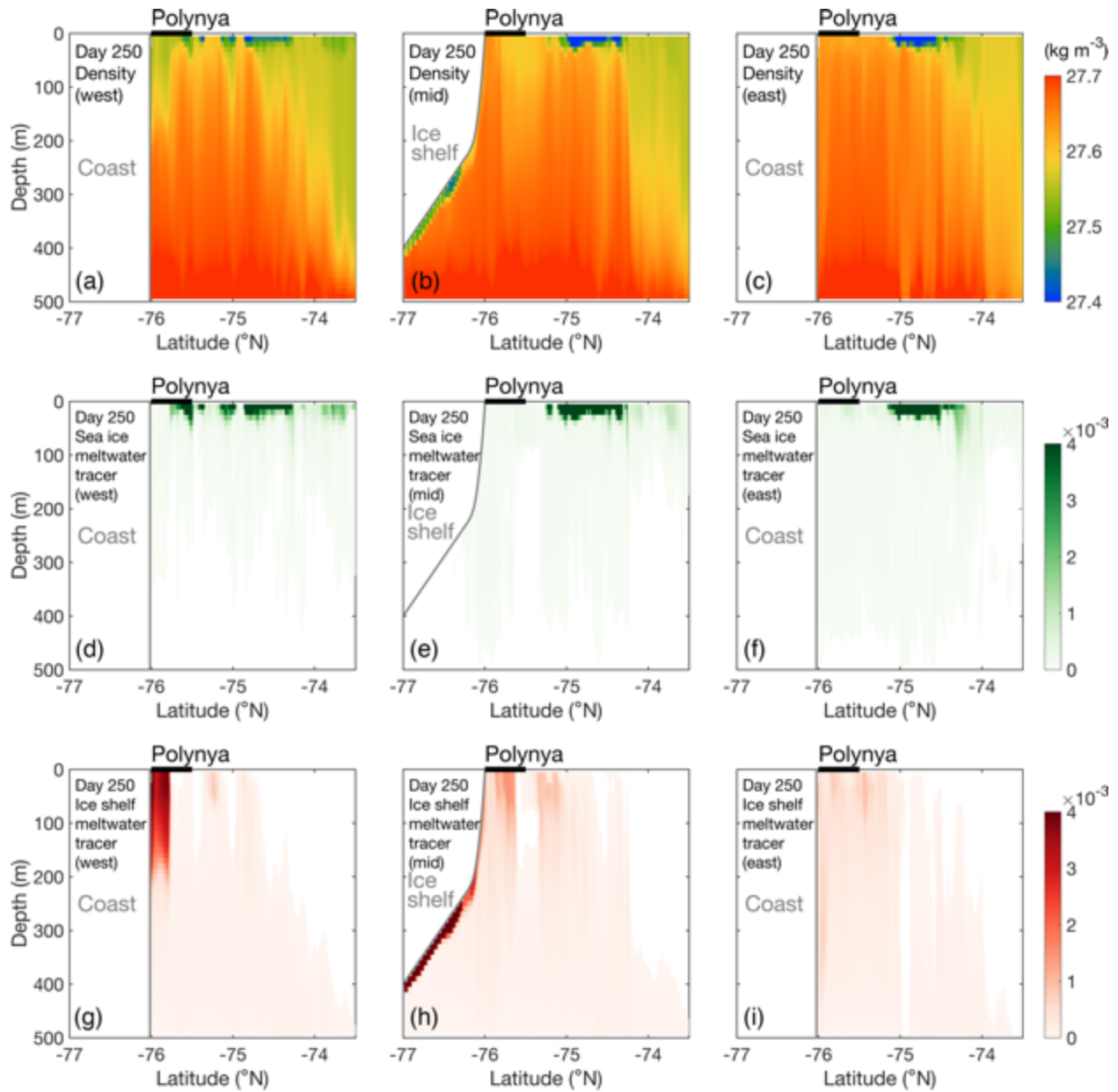


**Fig. 8.** Base Run A1: aerial view of selected model fields on Days 210, 230, and 250: (a-c) potential density (color) and velocity (arrows) at the surface (c); (d-f) potential energy anomaly integrated in the upper 100 m; (g-i) sea ice meltwater passive tracer concentration (color) and velocity (arrows) at the surface; (j-l) of ice shelf meltwater passive tracer concentration (color) and velocity (arrows) at the surface. The red dashed lines in (c) delineate the locations of three cross-shore transects in the west end, middle, and east end of the polynya as shown in Fig. 9.

561



562

563

564

565

566

**Fig. 9.** Cross-shore section of (a-c) potential density; (d-e) sea ice meltwater passive tracer concentration; (g-i) ice shelf meltwater passive tracer concentration in Base Run A1 on Day 250. The locations of these transects are outlined by dashed red lines in Fig. 8c.

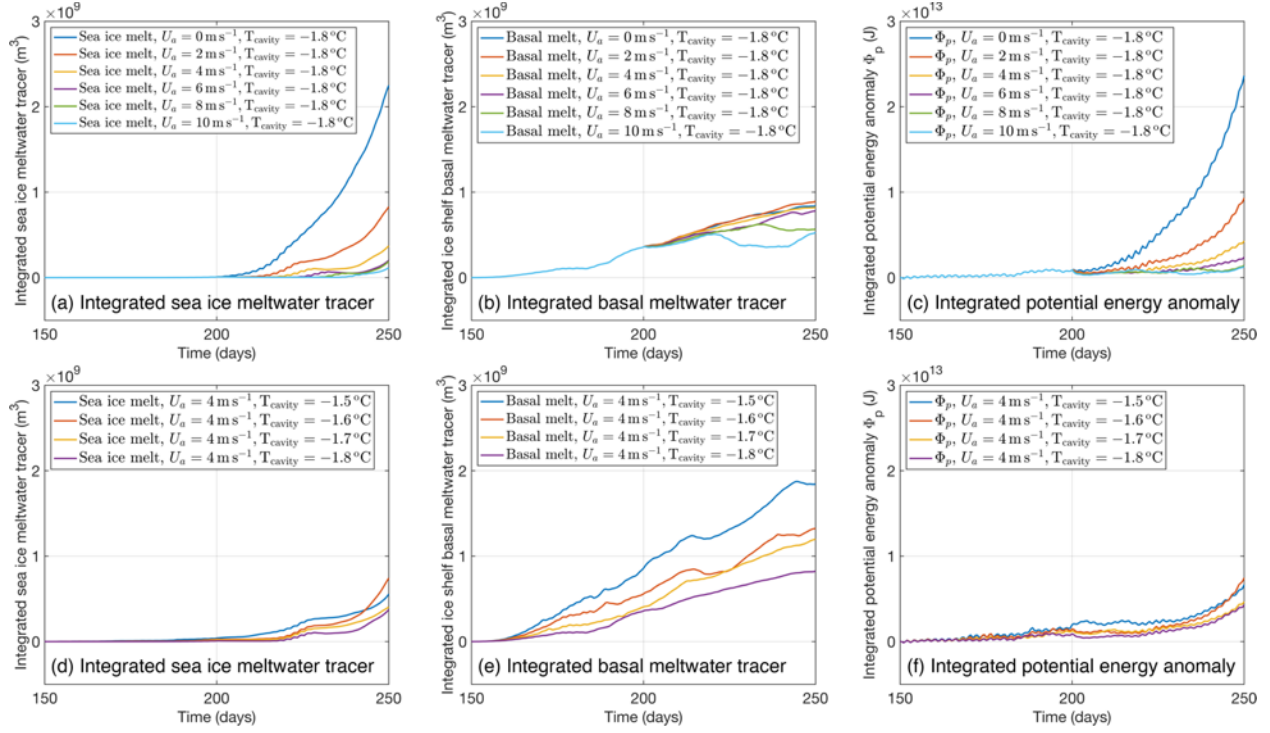


**Fig. 10.** Temporal evolution of the amount of sea ice passive tracer (a, d), the amount of ice shelf meltwater passive tracer (b, e), and potential energy anomaly (c, f) area-integrated in the upper 100 m of the polynya water column from sensitivity simulations S-AWind (a-c) and S-CWTemp.

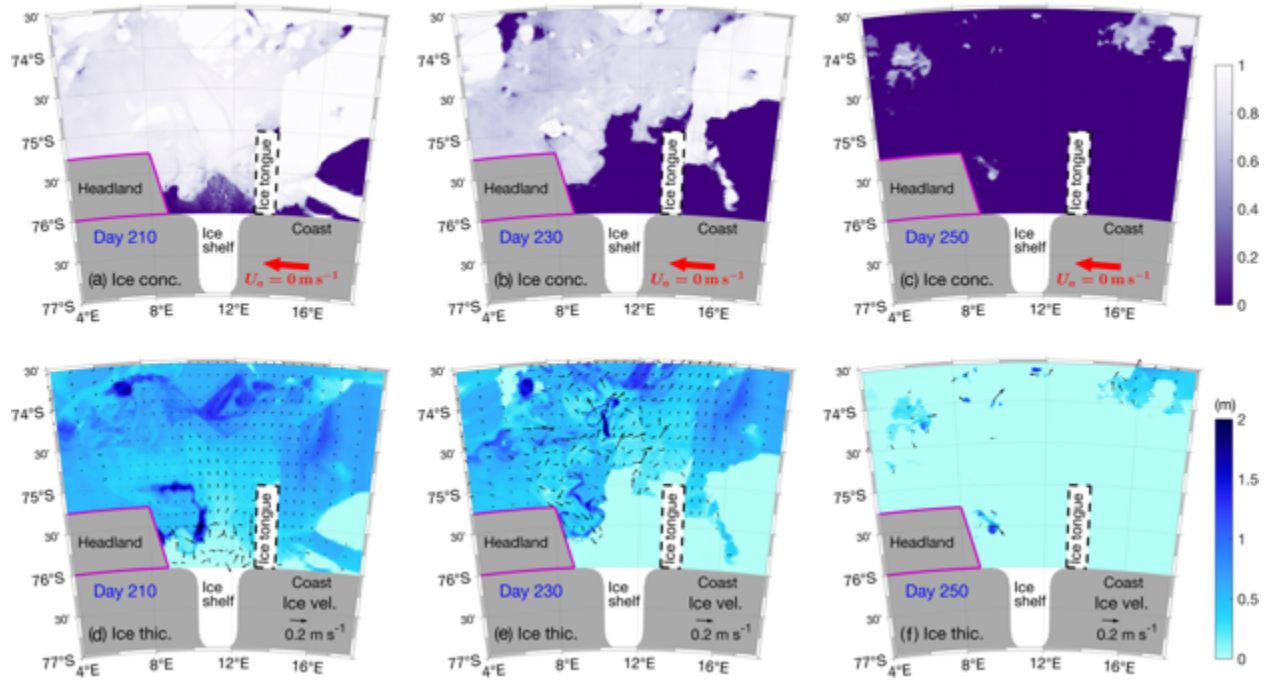


**Fig. 11.** Sensitivity run S-Awind with  $U_a = 0 \text{ m s}^{-1}$ : snapshots of the modeled (a-c) sea ice concentration; (b-d) sea ice thickness (color) and sea ice velocity (arrows) on Days 210 (left), 230 (middle), and 250 (right).



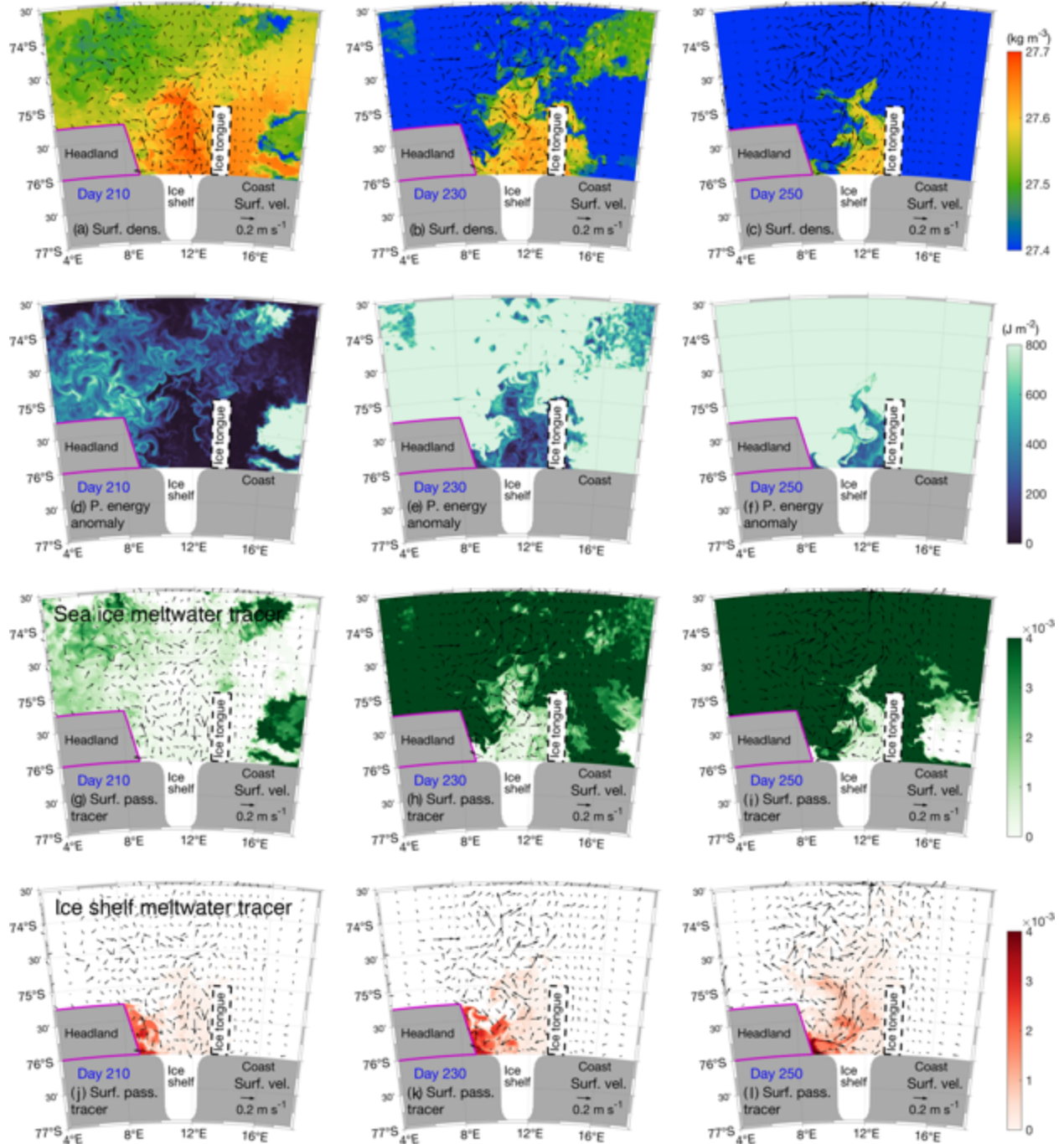
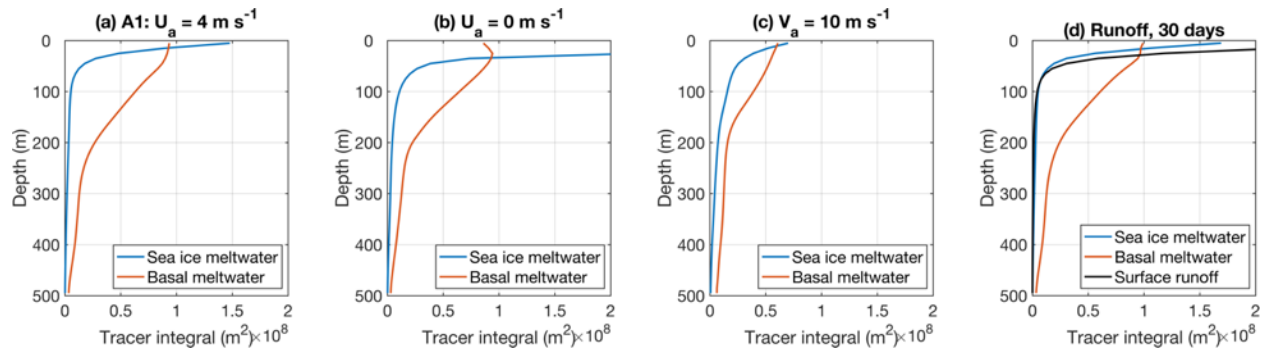


**Fig. 12.** Sensitivity run S-Awind with  $U_a = 0 \text{ m s}^{-1}$ : aerial view of selected model fields on Days 210, 230, and 250: (a-c) potential density (color) and velocity (arrows) at the surface (c); (d-f) potential energy anomaly integrated in the upper 100 m; (g-i) sea ice meltwater passive tracer concentration (color) and velocity (arrows) at the surface; (j-l) of ice shelf meltwater passive tracer concentration (color) and velocity (arrows) at the surface.

584



585

586

**Fig. 13.** Horizontally-integrated vertical profile of sea ice meltwater, ice shelf basal meltwater and surface runoff passive tracers in the polynya area from (a) Base Run A1; (b) case S-Awind with  $U_a = 0 \text{ m s}^{-1}$ ; (c) case S-Owind with  $V_a = 10 \text{ m s}^{-1}$ ; (d) case S-Srunoff with surface runoff lasting for 30 days.

590

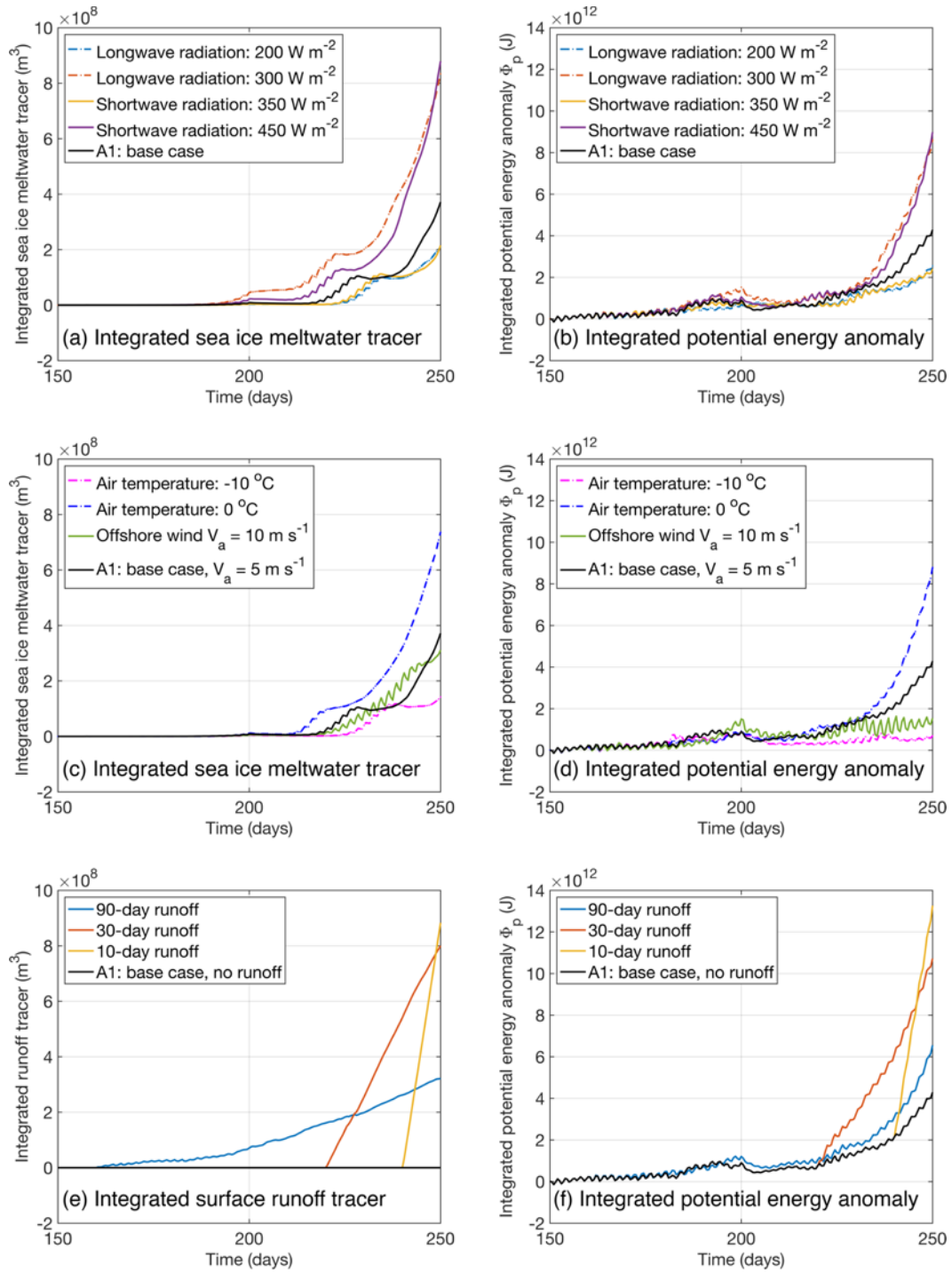
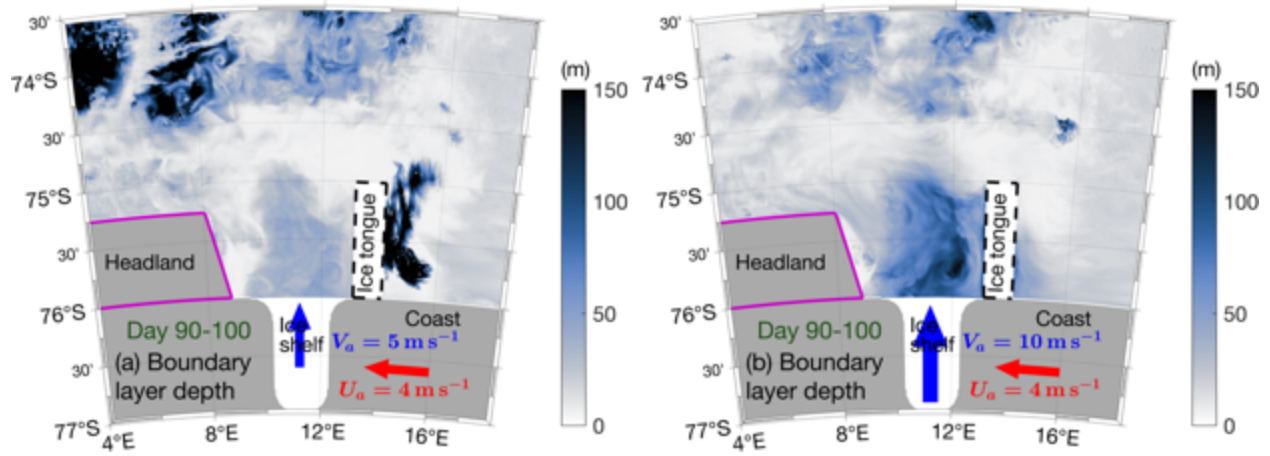


**Fig. 14.** Temporal evolution of the amount of sea ice meltwater passive tracer (a, c), surface runoff passive tracer (e), and potential energy anomaly (b, d, and f) area-integrated in the upper 100 m of the polynya water column from sensitivity simulations, S-LWRad and S-SWRad (a, b), S-Atemp and S-Owind (c, d), and S-Srunoff (e, f).

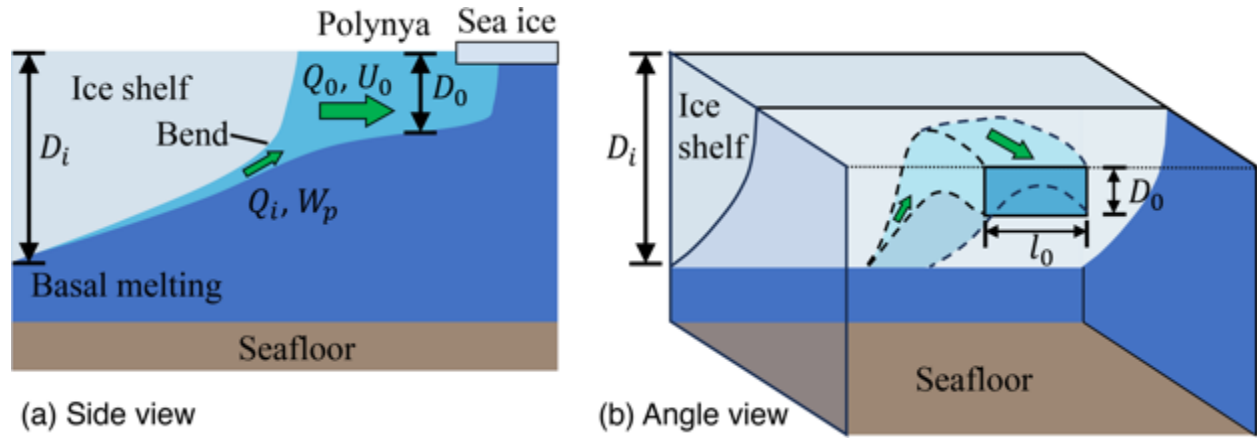
596



597

598 **Fig. 15.** Spatial distribution of the mean surface boundary layer depth during Day 240–250  
 599 in (a) the Base Run A1 with offshore wind speed  $V_a = 5 \text{ m s}^{-1}$  and (b) the sensitivity case with  $V_a$   
 600  $= 10 \text{ m s}^{-1}$ .

601



602

603 **Fig. 16.** Schematic illustration of the ice shelf basal meltwater plume in the (a) side view  
 604 and (b) angle view.

605

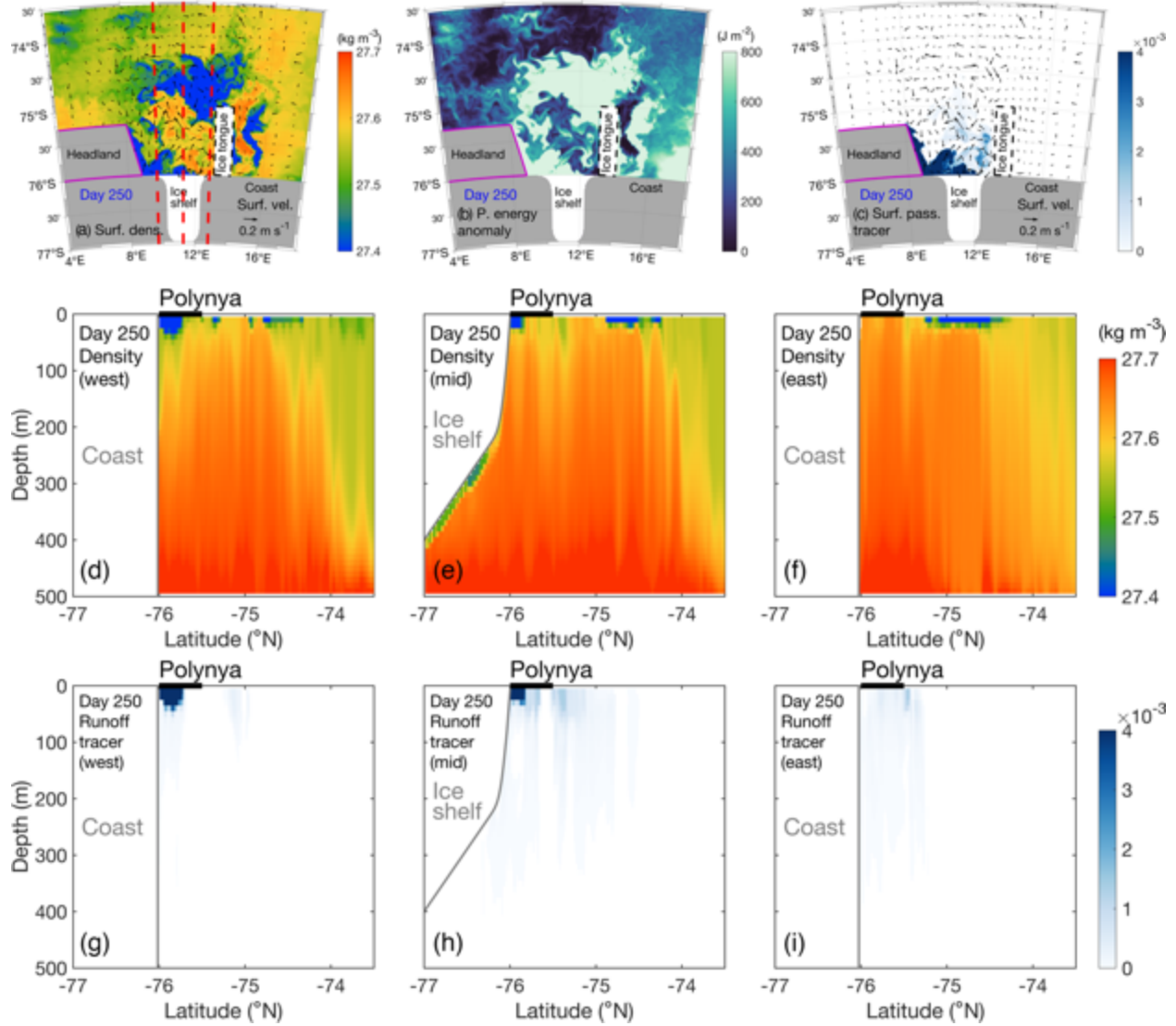


**Fig. 17.** Results of the S-Srunoff simulation with a 30-day surface runoff on Day 250: (a) surface potential density (color) and velocity (arrows); (b) potential energy anomaly integrated in the upper 100 m; (c) surface runoff passive tracer concentration (color) and surface velocity (arrows). The red dashed lines in (a) delineate the locations of three cross-shore transects of potential density (d-f) and surface runoff passive tracer concentration (g-i) in the west end, middle, and east end of the polynya.

## 4. Discussion

This study provides a qualitative understanding of the potential contribution of three major freshwater (buoyancy) sources, i.e., sea ice melt, ice shelf basal melt, and ice shelf surface runoff, on springtime near-surface restratification within an Antarctica coastal polynya, a process that is important for phytoplankton bloom. The effect of various factors, such as alongshore and offshore winds, air temperature, longwave and shortwave radiations, on the restratification are also considered. Our analysis demonstrates pronounced horizontal and vertical heterogeneity of newly developed stratification within the polynya water column. For instance, the western part of the polynya area tends to have lower surface densities due to accumulation of both sea ice or ice shelf meltwater there. In the vertical direction, two types of restratified layers appear in the western part of the polynya: a deeper restratified layer established by outflow of ice shelf basal meltwater and a shallower one resulting from sea ice meltwater. The shallower restratification is in the euphotic zone and thus biologically important. Moreover, surface runoff of the Antarctic ice shelf surface meltwater is highly uncertain in terms of its location, occurrence, duration, and magnitude. However, if occurs, it could greatly affect near-surface stratification in the western part of the polynya area, as vertical distribution of the surface runoff of the meltwater is similar to that of sea ice meltwater, while its horizontal distribution bears resemblance to that of ice shelf basal meltwater. Because characteristics of these different meltwaters vary across regions, their relative contributions to springtime polynya restratification can change from one polynya to another. The heterogeneity in the spatial distribution of meltwaters in a polynya region and the potential cross-polynya variation in their contribution highlight the need for detailed analyses to understand restratification dynamics in specific polynyas.

### 4.1. Horizontal Distribution of Meltwaters

Our analyses indicate that sea ice melt exerts a major influence on biologically important near-surface restratification in the coastal polynyas. As shown in Fig. 8, the springtime decrease in surface density and near-surface restratification coincide largely with the pattern of sea ice melt. This coincidence occurs in both the polynya and the area immediately offshore, but the timing and magnitude of the restratification differ spatially. The offshore region undergoes an earlier and more intense restratification, aligned with higher initial sea ice concentration there. Moreover, our

sensitivity simulations (Fig. 10a-c) shed light on the pivotal role of alongshore winds in modulating the volume of sea ice meltwater reaching the polynya area. Specifically, increasing the speed of alongshore winds causes some sea ice being pushed away and leads to a reduced volume of sea ice meltwater in the polynya area. This underlines the importance of the alongshore wind as a controlling factor for the springtime restratification and biological productivity in Antarctic coastal polynyas.

The spatial heterogeneity in the distributions of the different meltwaters is a key result of this study. Fig. 8 offers an illustration on how sea ice meltwater and ice shelf meltwaters are separated spatially. While the sea ice meltwater predominantly infiltrates the polynya area from the offshore and is carried by currents, both the ice shelf basal meltwater and surface runoff are more localized and concentrated on the western end of the polynya, as driven by the Coriolis force.

## 4.2. Vertical Distribution of Meltwaters

In the vertical direction, the meltwater sources also exhibit different pattern of distribution. Both sea ice meltwater and surface runoff concentrate at the surface as they are directly injected into the polynya surface. They can thus directly contribute to the near-surface restratification. However, an increase in the offshore wind speed could enhance vertical mixing and destroy the near-surface stratification, even though the overall amount of sea ice meltwater in the polynya area remained almost unchanged (Fig. 14c). When the offshore wind speed increases from 5 to 10 m s<sup>-1</sup>, the model shows a clear reduction in potential energy anomaly (Fig. 14d) and thickening of the surface boundary layer (Fig. 15). The same effect presumably applies to the near-surface stratification established by the surface runoff. This indicates a crucial role that offshore winds play in modulating boundary layer dynamics and thus the springtime near-surface restratification in the polynyas.

Another intriguing finding here pertains to the vertical mixing of ice shelf basal meltwater. Unlike sea ice meltwater or surface runoff, ice shelf basal meltwater exhibits a more uniform distribution throughout the upper ~200 m of the water column in the model. Both our numerical models and analytical scaling show a vertical length scale of the ice shelf basal meltwater outflow of  $O(100\text{ m})$ . This can be attributed to the mixing with the ambient water during its upward movement from the ice shelf cavity. It allows the ice shelf basal meltwater to spread more evenly



in the upper hundreds of meters, contrasting with the surface-confined distribution of sea ice and surface runoff meltwater. This result suggests that, even though ice shelf basal melt might contribute significantly to the freshwater content in the polynya region, it is not necessarily a major contributor to the near-surface stratification, a key factor of the springtime phytoplankton bloom in Antarctic coastal polynyas.

### 4.3. Implications on Biological Productivity

This study provides a qualitative understanding on how three types of meltwaters could contribute to the spring restratification in Antarctic coastal polynyas and how a number of physical factors could potentially affect that through modifying the meltwater distributions. The modeled spatial heterogeneity in polynya spring restratification is qualitatively consistent with the observed non-uniform distribution of chlorophyll-a concentration at the TNBP (Fig. 4). In areas where sea ice meltwater is prevalent, especially at the northwestern edge of the modeled polynya (the northern end of the TNBP), lower surface densities create a stable surface layer. Such condition is conducive for phytoplankton growth, as they enable the retention of newly produced biomass in the euphotic zone, thereby enhancing primary productivity. While part of the high chlorophyll-a concentration near the sea ice edge might result from sub-ice blooms, these blooms would be enhanced or sustained by the strong near-surface stratification there established by concentrated sea ice meltwater, which is consistent with our argument. The inhomogeneous distribution of phytoplankton growth might also shape the spatial distribution of zooplankton and higher trophic levels (e.g., Tachibana et al., 2023). In addition, the spatially concentrated distribution of ice shelf basal meltwater has a potential influence on the nutrient availability and cycling in the region, as the ice shelf basal meltwater is rich in iron, a major limiting factor for the phytoplankton growth in the region (Dinniman et al., 2020). Our model result suggests that nutrients provided by the basal meltwater are likely confined to a corner of the polynya near the coast and might not be immediately available to the larger polynya region. The surface mixed layer established by the basal meltwater is too deep ( $> 100$  m) to keep phytoplankton in the euphotic zone. Similarly, surface runoff of the ice shelf surface melt, while contributing to the formation of a shallow restratified layer near the surface, is confined horizontally in the coastal corner of the polynya. Hence, this runoff meltwater might also not be readily accessible to the rest of the polynya.

The configuration in this study is highly idealized, and settings of coastal polynyas around Antarctica are much more complicated and they change across polynyas. Factors that are neglected in this study, such as more complex coastline geometry, land-fast ice dynamics, sea ice boundary conditions, higher-frequency wind fluctuations, irregular shelf bathymetry, and ice shelf basal and surface topography, could modify distribution of the meltwaters, pattern of the near-surface restratification, and then biological productivity in an Antarctic coastal polynya. For instance, a recent study of the TNBP (Kim et al., 2023) shows that irregular shelf bathymetry, such as deep troughs, can affect circulation under the ice shelf and modify the CDW intrusion and rates of basal melting. However, because ice shelf basal melt contributes relatively little to the springtime near-surface restratification, we anticipate that the influence of shelf bathymetry on the restratification in coastal polynyas is weak. It is possible that irregular bathymetry affects shelf circulation and then the delivery of sea ice into the polynyas. This potential pathway of bathymetric influence is neglected in this study and should be addressed in future studies. Meanwhile, recently identified enhancement of lateral transport and mixing of basal meltwater during its ascent at the ice shelf front induced by small-scale ( $\sim 1$  km) centrifugal overturning instability (Garabato et al., 2017) is not considered here because the model resolution ( $\sim 1$  km) is not high enough to resolve the process. Moreover, in the Mertz Polynya, after the Mertz Glacier Tongue calving in 2010 (Lacarra et al., 2014; Snow et al., 2018), sea ice from upstream can flow alongshore into the polynya area, supplying sea ice meltwater into the polynya surface. This change in the sea ice boundary condition could enhance the near-surface restratification and associated spring bloom in the polynya. This contrasts with the TNBP, where the Drygalski Ice Tongue blocks the northward sea ice flow from the upstream into the polynya (Bromwich & Kurtz, 1984; Kurtz & Bromwich, 1985), reducing the availability of sea ice meltwater in spring. In the Amundsen Sea Polynya, the outflow of sea ice produced by the polynya can occasionally be blocked by the nearby iceberg chain and thus stay locally in the polynya (Macdonald et al., 2023), which could enhance surface restratification. Meanwhile, in the same region, significant CDW intrusion and basal melting from adjacent ice shelves (Randall-Goodwin et al., 2015) contribute substantially to the iron supply and enhance phytoplankton productivity in the polynya (Sherrell et al., 2015), a process that is not considered in this study. The difference in these polynyas indicates that understanding the resilience and adaptability of any Antarctic coastal polynya ecosystem in a rapidly changing climate, requires a thorough investigation of the detailed physical and biological processes with a full consideration

of the local complexity. This study provides a framework for future studies to examine the influence of different factors on the springtime restratification, a key process for the primary biological production in the polynyas.

## 5. Summary

In this study, we investigate the influences of atmospheric, oceanic, and sea ice and ice shelf processes on springtime restratification in Antarctic coastal polynyas. Utilizing a series of numerical sensitivity simulations, we explore the role of alongshore and offshore winds, ice shelf basal melt rate (through altering water temperature in the ice shelf cavity), and surface heat fluxes on the development of near-surface stratification that is crucial for phytoplankton blooms in the polynyas in early spring. One of our key findings relates to the spatial distribution of different types of meltwaters and the associated heterogeneity in near-surface restratification in the polynya region. Sea ice meltwater is predominantly influenced by alongshore winds and is largely concentrated in the offshore areas of the polynya. Meanwhile, sea ice melt in the polynya itself is less important, as the sea ice in the polynya has been transported offshore by the offshore winds. Sea ice meltwater in the polynya area is primarily carried from the offshore region into the polynya by ocean circulation, and offshore sea ice melt thus contributes significantly to restratification in the polynya region, particularly the outer polynya region. This is consistent with the observed peak chlorophyll-a concentration at the edge of the Terra Nova Bay Polynya in the spring. In contrast, ice shelf basal meltwater — although a major constituent of the meltwater volume within the polynya water column — is more mixed in the vertical direction due to strong mixing with the ambient water during its ascent. This results in a less important role of ice shelf basal meltwater in polynya near-surface restratification compared to sea ice meltwater. Surface runoff of the ice shelf surface meltwater, a potential buoyancy source of high uncertainty, exhibits a distinct distribution pattern in the polynya region, resembling sea ice meltwater in its vertical distribution but ice shelf basal meltwater in its horizontal nearshore concentration. Our model suggests that surface runoff, if occurs, could significantly contribute to the near-surface restratification in the western part of the modeled polynya through establishing a shallow surface layer of less dense water there.

Our analysis highlights the spatial heterogeneity in the distribution of meltwaters in the polynya water column and illustrates their different influences on the near-surface restratification

process. This spatial heterogeneity can potentially explain the inhomogeneous chlorophyll-a distributions in Antarctic coastal polynyas. In particular, results of this study are consistent with satellite observations in the Terra Nova Bay Polynya showing the highest springtime chlorophyll concentration near the polynya edge where the sea ice meltwater establishes the strongest near-surface stratification. Overall, using an idealized polynya model, this research provides insights on the springtime polynya restratification dynamics and their sensitivity to various physical factors, thereby deepening our understanding of these critical systems in the context of climate change. Future research will include the use of a realistic model to validate the findings presented in this study to examine the potential influence of other factors (e.g., more complex coastline geometry and ice shelf basal and surface topology) that are neglected in this work.

## Acknowledgments

This study is supported by the National Science Foundation through Grants OPP-1643901, OPP-1643735, OPP-2021245, and OPP-2205008. CW and WGZ are also supported by NASA through Grant 80NSSC23K0356.

## Data Availability Statement

The MODIS images were obtained from the Worldview tool from NASA's Earth Observing System Data and Information System at <https://worldview.earthdata.nasa.gov/>. The meteorological station data were downloaded from the University of Wisconsin-Madison Automatic Weather Station Program at <https://amrc.ssec.wisc.edu/data/ftp/pub/aws/q1h/2019/>. The AMPS data (Powers et al., 2012) were acquired from the NCAR Climate Data Gateway at <https://www.earthsystemgrid.org/dataset/ucar.mmm.amps.output.2019.07.07.html>. The GSHHG data (Wessel & Smith, 1996) were downloaded at <https://www.soest.hawaii.edu/pwessel/gshhg/>. The marine mammal data (Roquet et al., 2014; Roquet et al., 2021) were collected and made freely available at <https://www.seanoe.org/data/00343/45461/> by the International MEOP Consortium and the national programs that contribute to it. The PIPERS CTD data (Ackley et al., 2020) were obtained from the U.S. Antarctic Program Data Center at <https://www.usap-dc.org/view/dataset/601422>. The chlorophyll-a concentration data were acquired from the

PolarWatch ERDDAP data server maintained by NOAA at <https://polarwatch.noaa.gov/erddap/files/nedisVHNSQchlaDaily/>. The ASI sea ice concentration data (Spreen et al., 2008) were available from the University of Bremen at [https://data.seaice.uni-bremen.de/amr2/asi\\_daygrid\\_swath/s6250/netcdf/](https://data.seaice.uni-bremen.de/amr2/asi_daygrid_swath/s6250/netcdf/). The ERA5 data (Hersbach et al., 2020) were downloaded from the Copernicus Climate Change Service at <https://doi.org/10.24381/cds.adbb2d47>. The model code and scripts (Xu et al., 2023c) used in this study are available at <https://doi.org/10.5281/zenodo.8412090>.

## References

- Ackley, S. F., Stammerjohn, S., Maksym, T., Smith, M., Cassano, J., Guest, P., et al. (2020). Sea-ice production and air/ice/ocean/biogeochemistry interactions in the Ross Sea during the PIPERS 2017 autumn field campaign. *Annals of Glaciology*, 61(82), 181–195. <https://doi.org/10.1017/aog.2020.31>
- Alderkamp, A. C., Van Dijken, G. L., Lowry, K. E., Connelly, T. L., Lagerström, M., Sherrell, R. M., et al. (2015). Fe availability drives phytoplankton photosynthesis rates during spring bloom in the Amundsen Sea Polynya, Antarctica. *Elementa*, 3(C), 1–26. <https://doi.org/10.12952/journal.elementa.000043>
- Arrigo, K. R. (2007). Physical Control of Primary Productivity in Arctic and Antarctic Polynyas. In W. O. Smith & D. G. Barber (Eds.), *Polynyas: Windows to the World, Elsevier Oceanography Series* (Vol. 74, pp. 223–238). Elsevier, Amsterdam, The Netherlands. [https://doi.org/10.1016/S0422-9894\(06\)74007-7](https://doi.org/10.1016/S0422-9894(06)74007-7)
- Arrigo, K. R., & van Dijken, G. L. (2003). Phytoplankton dynamics within 37 Antarctic coastal polynya systems. *Journal of Geophysical Research: Oceans*, 108(8). <https://doi.org/10.1029/2002jc001739>
- Arrigo, K. R., Van Dijken, G. L., & Strong, A. L. (2015). Environmental controls of marine productivity hot spots around Antarctica. *Journal of Geophysical Research: Oceans*, 120(8), 5545–5565. <https://doi.org/10.1002/2015JC010888>
- Bell, R. E., Banwell, A. F., Trusel, L. D., & Kingslake, J. (2018). Antarctic surface hydrology and impacts on ice-sheet mass balance. *Nature Climate Change*, 8(12), 1044–1052. <https://doi.org/10.1038/s41558-018-0326-3>
- Bell, R. E., Chu, W., Kingslake, J., Das, I., Tedesco, M., Tinto, K. J., et al. (2017). Antarctic ice shelf potentially stabilized by export of meltwater in surface river. *Nature*, 544(7650), 344–348. <https://doi.org/10.1038/nature22048>

827 Bromwich, D. H., & Kurtz, D. D. (1984). Katabatic wind forcing of the Terra Nova Bay polynya.  
828 *Journal of Geophysical Research*, 89(C3), 3561. <https://doi.org/10.1029/JC089iC03p03561>

829 Budillon, G., & Spezie, G. (2000). Thermohaline structure and variability in the Terra Nova Bay  
830 polynya, Ross Sea. *Antarctic Science*, 12(4), 493–508.  
831 <https://doi.org/10.1017/S0954102000000572>

832 Ching, C. Y., Fernando, H. J. S., & Noh, Y. (1993). Interaction of a negatively buoyant line plume  
833 with a density interface. *Dynamics of Atmospheres and Oceans*, 19(1–4), 367–388.  
834 [https://doi.org/10.1016/0377-0265\(93\)90042-6](https://doi.org/10.1016/0377-0265(93)90042-6)

835 Dinniman, M. S., St-Laurent, P., Arrigo, K. R., Hofmann, E. E., & van Dijken, G. L. (2020).  
836 Analysis of Iron Sources in Antarctic Continental Shelf Waters. *Journal of Geophysical*  
837 *Research: Oceans*, 125(5), 1–19. <https://doi.org/10.1029/2019JC015736>

838 Garabato, A. C. N., Forryan, A., Dutrieux, P., Brannigan, L., Biddle, L. C., Heywood, K. J., et al.  
839 (2017). Vigorous lateral export of the meltwater outflow from beneath an Antarctic ice shelf.  
840 *Nature*, 542(7640), 219–222. <https://doi.org/10.1038/nature20825>

841 Galton-Fenzi, B. K., Hunter, J. R., Coleman, R., Marsland, S. J., & Warner, R. C. (2012). Modeling  
842 the basal melting and marine ice accretion of the Amery Ice Shelf. *Journal of Geophysical*  
843 *Research: Oceans*, 117(C9), n/a-n/a. <https://doi.org/10.1029/2012JC008214>

844 Hersbach, H., Bell, B., Berrisford, P., Hirahara, S., Horányi, A., Muñoz-Sabater, J., et al. (2020).  
845 The ERA5 global reanalysis. *Quarterly Journal of the Royal Meteorological Society*,  
846 146(730), 1999–2049. <https://doi.org/10.1002/qj.3803>

847 Kacimi, S., & Kwok, R. (2020). The Antarctic sea ice cover from ICESat-2 and CryoSat-2:  
848 freeboard, snow depth, and ice thickness. *The Cryosphere*, 14(12), 4453–4474.  
849 <https://doi.org/10.5194/tc-14-4453-2020>

850 Kim, T., Hong, J., Jin, E. K., Moon, J., Song, S., & Lee, W. S. (2023). Spatiotemporal variability  
851 in ocean-driven basal melting of cold-water cavity ice shelf in Terra Nova Bay, East  
852 Antarctica: roles of tide and cavity geometry. *Frontiers in Marine Science*, 10(September),  
853 1–14. <https://doi.org/10.3389/fmars.2023.1249562>

854 Kurtz, D. D., & Bromwich, D. H. (1985). A recurring, atmospherically forced polynya in Terra  
855 Nova Bay. In *Antarctic Research Series* (Vol. 43, pp. 177–201).  
856 <https://doi.org/10.1029/AR043p0177>

857 Lacarra, M., Houssais, M.-N., Herbaut, C., Sultan, E., & Beauverger, M. (2014). Dense shelf water  
858 production in the Adélie Depression, East Antarctica, 2004–2012: Impact of the Mertz Glacier  
859 calving. *Journal of Geophysical Research: Oceans*, 119(8), 5203–5220.  
860 <https://doi.org/10.1002/2013JC009124>

861 Li, Y., Ji, R., Jenouvrier, S., Jin, M., & Stroeve, J. (2016). Synchronicity between ice retreat and  
862 phytoplankton bloom in circum-Antarctic polynyas. *Geophysical Research Letters*, 43(5),  
863 2086–2093. <https://doi.org/10.1002/2016GL067937>

864 Linden, P. F., Lane-Serff, G. F., & Smeed, D. A. (1990). Emptying filling boxes: the fluid  
865 mechanics of natural ventilation. *Journal of Fluid Mechanics*, 212(1), 309.  
866 <https://doi.org/10.1017/S0022112090001987>

867 Long, M. C., Thomas, L. N., & Dunbar, R. B. (2012). Control of phytoplankton bloom inception  
868 in the Ross Sea, Antarctica, by Ekman restratification. *Global Biogeochemical Cycles*, 26(1),  
869 n/a-n/a. <https://doi.org/10.1029/2010GB003982>

870 Losch, M. (2008). Modeling ice shelf cavities in a z coordinate ocean general circulation model.  
871 *Journal of Geophysical Research*, 113(C8), C08043. <https://doi.org/10.1029/2007JC004368>

872 Macdonald, G. J., Ackley, S. F., Mestas-Nuñez, A. M., & Blanco-Cabanillas, A. (2023). Evolution  
873 of the dynamics, area, and ice production of the Amundsen Sea Polynya, Antarctica, 2016–  
874 2021. *The Cryosphere*, 17(2), 457–476. <https://doi.org/10.5194/tc-17-457-2023>

875 Malyarenko, A., Robinson, N. J., Williams, M. J. M., & Langhorne, P. J. (2019). A Wedge  
876 Mechanism for Summer Surface Water Inflow Into the Ross Ice Shelf Cavity. *Journal of*  
877 *Geophysical Research: Oceans*, 124(2), 1196–1214. <https://doi.org/10.1029/2018JC014594>

878 Marshall, J., Adcroft, A., Hill, C., Perelman, L., & Heisey, C. (1997). A finite-volume,  
879 incompressible navier stokes model for, studies of the ocean on parallel computers. *Journal*  
880 *of Geophysical Research C: Oceans*, 102(C3), 5753–5766.  
881 <https://doi.org/10.1029/96JC02775>

882 Morales Maqueda, M. A., Willmott, A. J., & Biggs, N. R. T. (2004). Polynya Dynamics: a Review  
883 of Observations and Modeling. *Reviews of Geophysics*, 42(1).  
884 <https://doi.org/10.1029/2002RG000116>

885 Moreau, S., Lannuzel, D., Janssens, J., Arroyo, M. C., Corkill, M., Cougnon, E., et al. (2019). Sea  
886 Ice Meltwater and Circumpolar Deep Water Drive Contrasting Productivity in Three  
887 Antarctic Polynyas. *Journal of Geophysical Research: Oceans*, 124(5), 2943–2968.  
888 <https://doi.org/10.1029/2019JC015071>

889 Orlanski, I. (1976). A simple boundary condition for unbounded hyperbolic flows. *Journal of*  
890 *Computational Physics*, 21(3), 251–269. [https://doi.org/10.1016/0021-9991\(76\)90023-1](https://doi.org/10.1016/0021-9991(76)90023-1)

891 Powers, J. G., Manning, K. W., Bromwich, D. H., Cassano, J. J., & Cayette, A. M. (2012). A  
892 Decade of Antarctic Science Support Through AMPS. *Bulletin of the American*  
893 *Meteorological Society*, 93(11), 1699–1712. <https://doi.org/10.1175/BAMS-D-11-00186.1>

894 Rack, W., Price, D., Haas, C., Langhorne, P. J., & Leonard, G. H. (2020). Sea Ice Thickness in the  
895 Western Ross Sea. *Geophysical Research Letters*. <https://doi.org/10.1029/2020GL090866>

896 Randall-Goodwin, E., Meredith, M. P., Jenkins, A., Yager, P. L., Sherrell, R. M., Abrahamsen, E.  
897 P., et al. (2015). Freshwater distributions and water mass structure in the Amundsen Sea  
898 Polynya region, Antarctica. *Elementa: Science of the Anthropocene*, 3, 1–22.  
899 <https://doi.org/10.12952/journal.elementa.000065>

900 Roquet, F., Guinet, C., Charrassin, J.-B., Costa, D., Kovacs, K., Lydersen, C., et al. (2021). MEOP-  
901 CTD in-situ data collection: a Southern ocean Marine-mammals calibrated sea water  
902 temperatures and salinities observations. [Dataset]. *SEANOE*, accessed 7 December 2021.  
903 <https://doi.org/10.17882/45461>

904 Roquet, F., Williams, G., Hindell, M. A., Harcourt, R., McMahon, C., Guinet, C., et al. (2014). A  
905 Southern Indian Ocean database of hydrographic profiles obtained with instrumented  
906 elephant seals. *Scientific Data*, 1(1), 140028. <https://doi.org/10.1038/sdata.2014.28>

907 Rusciano, E., Budillon, G., Fusco, G., & Spezie, G. (2013). Evidence of atmosphere-sea ice-ocean  
908 coupling in the Terra Nova Bay polynya (Ross Sea-Antarctica). *Continental Shelf Research*,  
909 61–62, 112–124. <https://doi.org/10.1016/j.csr.2013.04.002>

910 Schofield, O., Brown, M., Kohut, J., Nardelli, S., Saba, G., Waite, N., & Ducklow, H. (2018).  
911 Changes in the upper ocean mixed layer and phytoplankton productivity along the West  
912 Antarctic Peninsula. *Philosophical Transactions of the Royal Society A: Mathematical,*  
913 *Physical and Engineering Sciences*, 376(2122). <https://doi.org/10.1098/rsta.2017.0173>

914 Sherrell, R. M., Lagerström, M. E., Forsch, K. O., Stammerjohn, S. E., & Yager, P. L. (2015).  
915 Dynamics of dissolved iron and other bioactive trace metals (Mn, Ni, Cu, Zn) in the  
916 Amundsen Sea Polynya, Antarctica. *Elementa: Science of the Anthropocene*, 3, 1–27.  
917 <https://doi.org/10.12952/journal.elementa.000071>

918 Silvano, A., Rintoul, S. R., Peña-Molino, B., Hobbs, W. R., Van Wijk, E., Aoki, S., et al. (2018).  
919 Freshening by glacial meltwater enhances melting of ice shelves and reduces formation of  
920 Antarctic Bottom Water. *Science Advances*, 4(4). <https://doi.org/10.1126/sciadv.aap9467>

921 Simpson, J. H., Brown, J., Matthews, J., & Allen, G. (1990). Tidal Straining, Density Currents,  
922 and Stirring in the Control of Estuarine Stratification. *Estuaries*, 13(2), 125.  
923 <https://doi.org/10.2307/1351581>

924 Smith Jr., W. O., & Barber, D. G. (2007). *Polynyas: Windows to the World* (Vol. 74). Elsevier,  
925 Amsterdam, The Netherlands, 474 pp. [https://doi.org/10.1016/S0422-9894\(06\)X7400-7](https://doi.org/10.1016/S0422-9894(06)X7400-7)

926 Snow, K., Rintoul, S. R., Sloyan, B. M., & Hogg, A. M. C. (2018). Change in Dense Shelf Water  
927 and Adélie Land Bottom Water Precipitated by Iceberg Calving. *Geophysical Research*  
928 *Letters*, 45(5), 2380–2387. <https://doi.org/10.1002/2017GL076195>

929 Spreen, G., Kaleschke, L., & Heygster, G. (2008). Sea ice remote sensing using AMSR-E 89-GHz  
930 channels. *Journal of Geophysical Research*, 113(C2), C02S03.  
931 <https://doi.org/10.1029/2005JC003384>



- 932 Stevens, C., Sang Lee, W., Fusco, G., Yun, S., Grant, B., Robinson, N., & Hwang, C. Y. (2017).  
 933 The influence of the Drygalski Ice Tongue on the local ocean. *Annals of Glaciology*, 58(74),  
 934 51–59. <https://doi.org/10.1017/aog.2017.4>
- 935 Tachibana, A., Ohkubo, Y., Matsuno, K., Takahashi, K. D., Makabe, R., & Moteki, M. (2023).  
 936 Interannual and spatial variation in small zooplankton off Vincennes Bay, East Antarctica.  
 937 *Polar Biology*, 46(9), 915–932. <https://doi.org/10.1007/s00300-023-03174-0>
- 938 Vaillancourt, R. D., Sambrotto, R. N., Green, S., & Matsuda, A. (2003). Phytoplankton biomass  
 939 and photosynthetic competency in the summertime Mertz Glacier region of East Antarctica.  
 940 *Deep-Sea Research Part II: Topical Studies in Oceanography*, 50(8–9), 1415–1440.  
 941 [https://doi.org/10.1016/S0967-0645\(03\)00077-8](https://doi.org/10.1016/S0967-0645(03)00077-8)
- 942 Wang, C., Chant, R. J., & Jackson, R. H. (2023). Parameterizing Subglacial Discharge in Modeling  
 943 Buoyancy Driven Flow in Tidewater Glacier Fjords. *Journal of Geophysical Research:*  
 944 *Oceans*, 128(8), 1–21. <https://doi.org/10.1029/2023JC019924>
- 945 Wessel, P., & Smith, W. H. F. (1996). A global, self-consistent, hierarchical, high-resolution  
 946 shoreline database. *Journal of Geophysical Research: Solid Earth*, 101(B4), 8741–8743.  
 947 <https://doi.org/10.1029/96JB00104>
- 948 Xu, Y., Zhang, W. G., Maksym, T., Ji, R., & Li, Y. (2023a). Stratification Breakdown in Antarctic  
 949 Coastal Polynyas. Part I: Influence of Physical Factors on the Destratification Time Scale.  
 950 *Journal of Physical Oceanography*, 53(9), 2047–2067. [https://doi.org/10.1175/JPO-D-22-](https://doi.org/10.1175/JPO-D-22-0218.1)  
 951 0218.1
- 952 Xu, Y., Zhang, W. G., Maksym, T., Ji, R., & Li, Y. (2023b). Stratification Breakdown in Antarctic  
 953 Coastal Polynyas. Part II: Influence of an Ice Tongue and Coastline Geometry. *Journal of*  
 954 *Physical Oceanography*, 53(9), 2069–2088. <https://doi.org/10.1175/JPO-D-22-0219.1>
- 955 Xu, Y., Zhang, W. G., Maksym, T., Ji, R., Li, Y., & Walker, C. (2023c). Model code and scripts  
 956 in support of manuscript “Influence of Physical Factors on Restratisation of the Upper  
 957 Water Column in Antarctic Coastal Polynyas”. [Software]. *Zenodo*.  
 958 <https://zenodo.org/doi/10.5281/zenodo.8412090>